

# The effects of galaxy shape and rotation on the X-ray haloes of early-type galaxies – II. Numerical simulations

Andrea Negri,<sup>★</sup> Silvia Posacki, Silvia Pellegrini and Luca Ciotti

*Department of Physics and Astronomy, University of Bologna, viale Berti Pichat 6/2, I-40127 Bologna, Italy*

Accepted 2014 September 4. Received 2014 September 1; in original form 2014 May 30

## ABSTRACT

By means of high-resolution 2D hydrodynamical simulations, we study the evolution of the hot interstellar medium (ISM) for a large set of early-type galaxy models, characterized by various degrees of flattening and internal rotation. The galaxies are described by state-of-the-art axisymmetric two-component models, tailored to reproduce real systems; the dark matter haloes follow the Navarro–Frenk–White or the Einasto profile. The gas is produced by the evolving stars, and heated by Type Ia supernovae. We find that, in general, the rotation field of the ISM in rotating galaxies is very similar to that of the stars, with a consequent negligible heating contribution from thermalization of the ordered motions. The relative importance of flattening and rotation in determining the final X-ray luminosity  $L_X$  and temperature  $T_X$  of the hot haloes is a function of the galactic mass. Flattening and rotation in low-mass galaxies favour the establishment of global winds, with the consequent reduction of  $L_X$ . In medium- to high-mass galaxies, flattening and rotation are not sufficient to induce global winds; however, in the rotating models, the nature of the gas flows is deeply affected by conservation of angular momentum, resulting in a reduction of both  $L_X$  and  $T_X$ .

**Key words:** methods: numerical – galaxies: elliptical and lenticular, cD – galaxies: ISM – galaxies: kinematics and dynamics – X-rays: galaxies – X-rays: ISM.

## 1 INTRODUCTION

Early-type galaxies (ETGs) are embedded in hot ( $10^6$ – $10^7$  K), X-ray-emitting gaseous haloes (Fabbiano 1989; O’Sullivan, Forbes & Ponman 2001), produced mainly by stellar winds and heated by Type Ia supernovae (SNIa) explosions and by the thermalization of stellar motions. In particular, the thermalization of stellar motions is due to the interaction between the stellar and SNIa ejecta and the pre-existing hot interstellar medium (ISM) (e.g. Parriott & Bregman 2008). A number of different astrophysical phenomena determine the X-ray properties of the hot ISM, such as stellar population evolution, galaxy structure and internal kinematics, AGN presence and environmental effects. In particular, one of the empirical discoveries that followed the analysis of first X-ray data of ETGs was the sensitivity of the hot gas content to major galaxy properties as the shape of the mass distribution, and the mean rotation velocity of the stellar component (see Mathews & Brighenti 2003; Kim & Pellegrini 2012 for a full discussion of the most relevant observational and theoretical aspects concerning the X-ray haloes). From *Einstein* observations, it was found that on average, at any fixed optical luminosity  $L_B$ , rounder systems had larger total X-ray luminosity  $L_X$  and  $L_X/L_B$  (a measure of the galactic hot gas content) than flatter ETGs and S0 galaxies (Eskridge, Fabbiano & Kim 1995). More-

over, galaxies with axial ratio close to unity spanned the full range of  $L_X$ , while flat systems had  $L_X \lesssim 10^{41}$  erg s<sup>-1</sup>. This result was not produced by flat galaxies having a lower  $L_B$  with respect to round ETGs, since it held even in the range of  $L_B$  where the two shapes coexist (Pellegrini 1999). Moreover, it was found that  $L_X/L_B$  can be high only in slowly rotating galaxies, and is limited to low values for fast-rotating ones (Pellegrini, Held & Ciotti 1997; Sarzi et al. 2010). The relationship between  $L_X$  and shape/rotation was reconsidered, confirming the above trends, for the *ROSAT* PSPC sample (Pellegrini 2012), and for the *Chandra* sample (Boroson, Kim & Fabbiano 2011; Li et al. 2011; Sarzi et al. 2013). In particular, Sarzi et al. (2013), after confirming that slow rotators generally have the largest  $L_X$  and  $L_X/L_B$  values, also found that their gas temperature  $T_X$  values are consistent just with the thermalization of the stellar kinetic energy, estimated from  $\sigma_e$  (the luminosity-averaged stellar velocity dispersion within the effective radius  $R_e$ ). Fast rotators, instead, have generally lower  $L_X$  and  $L_X/L_B$  values, and the more so the larger their degree of rotational support; the  $T_X$  values of fast rotators keep below 0.4 keV and do not scale with  $\sigma_e$ . Therefore, there seems to be a dependence of the hot gas content and temperature on the galactic shape and internal dynamics. The investigation of the origin of this still poorly understood sensitivity is the goal of this paper.

Theoretically, different possibilities have been proposed, and explored both analytically (Ciotti & Pellegrini 1996, hereafter CP96;

<sup>★</sup>E-mail: [andrea.negri@unibo.it](mailto:andrea.negri@unibo.it)

Posacki, Pellegrini & Ciotti 2013, hereafter P13) and numerically (Brighenti & Mathews 1996; D’Ercole & Ciotti 1998, hereafter DC98; Negri, Ciotti & Pellegrini 2014, hereafter N14). The proposed explanations can be classified in two broad categories: the *energetic* ones and the *hydrodynamical* ones. Of course, the difference is not sharp, as the flow energetics affects the hydrodynamical evolution, and different hydrodynamical configurations lead to different redistributions of the energy available.

Explanations based on energetic effects suppose that the ISM in flat and rotating galaxies is less bound than in more round and non-rotating galaxies of similar luminosity (and so of similar SNIa energy input) so that in the former objects the ISM is more prone to develop a global/partial galactic wind, with the consequent decrease of  $L_X$ . A subdivision of energetic explanations is represented by consideration of *flattening* effects versus *rotational* effects. The flattening explanation requires that flat galaxies have shallower potential wells than rounder galaxies of similar luminosity, so the gas is less bound (independently of the galaxy kinematical support, ordered rotation or velocity dispersion). In this scenario, the X-ray underluminosity of rotating galaxies is just a by-product of the fact that fast rotation can be associated only with significant flattening. The rotational explanation, instead, assumes that the gas injected in the galaxy retains the stellar streaming motion, and so it is less bound in rotating galaxies than in velocity-dispersion-supported galaxies of similar shape: the correlation of X-ray underluminosity with galaxy flattening is now a by-product of the fact that rotating galaxies are generally flat. Note that in this explanation the thermalization of ordered ISM velocities is low, and then the ISM also lacks the corresponding energetic input; so the two effects (lower effective binding energy but also lower heating) are in competition. Indeed, the stellar random kinetic energy is always supplied to the ISM, while the thermalization of the ordered kinetic energy depends on the relative motion between the stellar population and the ISM (see also Pellegrini 2011; P13). P13 proposed that a lower energy injection at fixed  $L_B$ , due to the lack of thermalization of stellar streaming motions, could explain the lower  $T_X$  of rotating galaxies. The energetic scenario has been explored analytically in CP96 by using two-component Miyamoto–Nagai models, and in P13 by building a wide set of more realistic ETG models, with different flattened structures and kinematics. These works showed that the binding energy of the gas depends on the procedure adopted to ‘flatten’ the galaxy models, and that rotation affects also the hot gas temperature. Preliminary numerical results for S0 galaxies suggest a low thermalization in rotating systems (N14).

Explanations based on hydrodynamical effects are less direct. In this scenario, the rotation of the gas injected in the galaxy leads to hydrodynamical configurations of the ISM that, for different but co-operating reasons associated with angular momentum conservation, are less X-ray luminous than in non-rotating systems. For example, the gas density in the central galactic region is lower in rotating models, where a rotationally supported cold disc forms, than in non-rotating ones, where the gas flows straight to the centre, forming a hot, dense core. Thus, the X-ray faintness is not due to the onset of galactic winds, but to redistribution of the gas inside the galaxy. Now rotation is the main driver of X-ray underluminosity, and correlation with galaxy flattening is a by-product. Exploratory numerical simulations (N14) further showed that the X-ray underluminosity of flat objects could be due to hydrodynamical effects associated with angular momentum conservation of gas injected at large radii for massive galaxies, but it is more and more due to energetic reasons for low-mass systems.

Empirically, due to the difficulty to observationally disentangle purely rotational and purely flattening effects, it is not easy to draw a clear cut between the two broad explanations illustrated above. First of all, since rotation is dependent on flattening, only galaxies sufficiently flattened are expected to rotate significantly. Secondly, given that the observed flattening in real objects is affected by projection effects, intrinsically flattened galaxies, if observed face-on (FO), can be found in the region occupied by rounder galaxies in the ellipticity–X-ray-properties diagrams.

For these reasons, by using high-resolution 2D hydrodynamical simulations of gas flows in realistic, state-of-the-art models of ETGs, we study this long-standing issue of the X-ray underluminosity of flat and rotating galaxies, together with the properties of their  $T_X$  values. In order to derive robust conclusions, we perform a large-scale exploration of the parameter space of realistic (axisymmetric) galaxy models characterized by different stellar mass, intrinsic flattening, distribution of dark matter and internal kinematics. In particular, the galaxy flattening is supported by ordered rotation (isotropic rotators) or by tangential anisotropy. All galaxy models are constructed by using the Jeans code described in P13, and are tailored to reproduce the observed properties and scaling laws of ETGs. These simulations also allow us to test how much simple energetic estimates (such as those of CP96 and P13) can be trustworthy in interpreting the global properties of the hot gaseous X-ray coronae.

The paper is organized as follows. In Section 2, we describe the main ingredients of the simulations, such as the galaxy models and the input physics. The main results are presented in Section 3, and Section 4 summarizes the conclusions.

## 2 THE SIMULATIONS

### 2.1 The galaxy models

For the simulations, we adopt axisymmetric two-component galaxy models, where the stellar component can have different intrinsic flattening, while for simplicity the DM halo is kept spherical. In particular, the stellar component is described by the deprojection (Mellier & Mathez 1987) of the de Vaucouleurs (1948) law, generalized for ellipsoidal axisymmetric distributions,

$$\rho_*(R, z) = \rho_0 \xi^{-0.855} \exp(-\xi^{1/4}), \quad (1)$$

with

$$\rho_0 = \frac{M_* b^{12}}{16\pi q R_{e0}^3 \Gamma(8.58)}, \quad \xi = \frac{b^4}{R_{e0}} \sqrt{R^2 + \frac{z^2}{q^2}}, \quad (2)$$

where  $(R, \varphi, z)$  are the cylindrical coordinates and  $b \simeq 7.67$ . The flattening is controlled by the parameter  $q \leq 1$ , so that the minor axis is aligned with the  $z$ -axis.  $R_{e0}$  is the projected half-mass radius (effective radius) when the galaxy is seen FO; for an edge-on (EO) view, the circularized effective radius is  $R_e = R_{e0} \sqrt{q}$ . In the simulations, we restrict to  $q$  values of (1, 0.6, 0.3), corresponding to E0, E4 and E7 galaxies when seen EO. For the DM halo, we adopt the NFW (Navarro, Frenk & White 1997) or the Einasto (1965) profiles.

All models belong to two different *sets*, defined by the specific profile of the DM halo. The first set is characterized by an untruncated NFW profile

$$\rho_h(r) = \frac{\rho_{\text{crit}} \delta_c r_h}{r(1 + r/r_h)^2}, \quad (3)$$

where  $\rho_{\text{crit}} = 3H^2/8\pi G$  is the critical density for closure. We refer to the DM mass enclosed within  $r_{200}$  (the radius of a sphere of mean interior density 200  $\rho_{\text{crit}}$ ) as to the halo mass  $M_{\text{h}}$ . Following Navarro et al. (1997),

$$\delta_c = \frac{200}{3} \frac{c^3}{\ln(1+c) - c/(1+c)}, \quad c \equiv \frac{r_{200}}{r_{\text{h}}}. \quad (4)$$

The models in the second set are embedded in an Einasto profile

$$\rho_{\text{h}}(r) = \rho_c e^{d_n - x}, \quad x \equiv d_n \left( \frac{r}{r_{\text{h}}} \right)^{1/n}, \quad (5)$$

where  $\rho_c$  is the density at the spatial half-mass radius  $r_{\text{h}}$ ,  $n$  is a free parameter and

$$d_n \simeq 3n - \frac{1}{3} + \frac{8}{1215n} \quad (6)$$

(Retana-Montenegro et al. 2012). The total gravitational field is computed by using the code described in P13, and the same code is also used to solve numerically the Jeans equations for the velocity fields of the stars, under the implicit assumption of a two-integral distribution function. Ordered and random motions in the azimuthal direction are described using the Satoh (1980)  $k$ -decomposition. Following P13, the model parameters are tuned to reproduce the Faber–Jackson and the size–luminosity relations as given by Desroches et al. (2007) for  $\approx 10^5$  ETGs in the SDSS; the stellar mass-to-light ratios adopted pertain to a 12 Gyr old stellar population with a Kroupa initial mass function (Maraston 2005).

In each of the two sets, we consider different *families* of models, built following the procedure described in P13 (sections 3.3 and 3.4). Here, we just recall the main steps. Each family is associated with a spherical galaxy, which we call the ‘progenitor’. The progenitor structural parameters are determined by assigning  $\sigma_{\text{e8}}$  (the aperture luminosity-weighted velocity dispersion within  $R_{\text{e}}/8$ ), and then deriving the luminosity and effective radius  $R_{\text{e}}$  of the galaxy from the scaling laws cited above. Then, from a chosen stellar mass-to-light ratio, the stellar mass  $M_*$  is derived. Finally, the parameters of the DM halo are determined in order to reproduce the assumed  $\sigma_{\text{e8}}$  and fixing  $M_{\text{h}}/M_* \simeq 20$  (Behroozi, Wechsler & Conroy 2013). In the NFW set, these constraints produce  $r_{\text{h}} \simeq 2R_{\text{e}}$ ,  $22 \lesssim c \lesssim 37$  and a DM fraction  $f_{\text{DM}}$  within a sphere of radius  $R_{\text{e}}$  of  $\simeq 0.6$  for the spherical progenitors. For the Einasto set, we fix  $n = 6$ , and we find that  $r_{\text{h}} \simeq 20R_{\text{e}}$ , and  $f_{\text{DM}} \simeq 0.56$  for the spherical progenitor.

In each of the two sets, we considered three values of  $\sigma_{\text{e8}}$  for the spherical progenitors, i.e. 200, 250 and 300  $\text{km s}^{-1}$ . Therefore, each of the two sets is made of three families of models, for a total of six spherical progenitors. Table 1 lists all the relevant parameters characterizing the progenitors galaxy models for both sets. The flattened descendants of each progenitor with intrinsic flattening of E4 ( $q = 0.6$ ) and E7 ( $q = 0.3$ ) are derived as follows. We produce two flattened models for each value of  $q$ . The first flattened model is called ‘face-on built’ (hereafter FO-built), since, when observed FO, its  $R_{\text{e}}$  is the same as that of the spherical progenitor; this requires FO-built-flattened models to be more and more concentrated as  $q$  decreases ( $\rho_* \propto q^{-1}$ ). The second flattened model instead, when seen EO, has the same circularized  $R_{\text{e}}$  of the spherical progenitor; thus, we call it ‘edge-on built’ (hereafter EO-built); this property makes the EO-built models expand with decreasing  $q$  ( $\rho_* \propto \sqrt{q}$ ). Therefore, a spherical progenitor with a given value of  $\sigma_{\text{e8}}$  produces four flat galaxies: two E4 models (FO and EO built) and two E7 models (FO and EO built). As a further step, in order to study the effects of galaxy rotation, we assume two kinematical supports for each flattened system: one corresponding to a velocity-dispersion-

supported galaxy (VD models), and the other one to an isotropic rotator (IS models). These two configurations are obtained by setting the Satoh parameter  $k$  equal to 0 and 1, respectively (see P13, equations B3 and B4). In the flattening procedure, the DM halo is maintained fixed to that of the progenitor. Note that our flattened models are representative of ETGs since they are consistent with their observed properties. We indeed checked for models lying outside the observed scatter of the scaling laws, but our adopted flattening procedure is quite robust in producing acceptable models, so that we retained all of them.

Summarizing, from each spherical progenitor of given  $\sigma_{\text{e8}}$ , eight flattened models are obtained (see Table 1), and we refer to this group of nine galaxy models as to a family. All models belonging to a family can be identified either by the  $\sigma_{\text{e8}}$  value of the spherical progenitor, or by their stellar mass  $M_*$  (or  $B$  luminosity), or DM halo mass; note however that while these last three quantities are kept constant within a family, the  $\sigma_{\text{e8}}$  of the descendants varies. Indeed, the modification of stellar structure involves a change in the stellar kinematics, and so in the value of  $\sigma_{\text{e8}}$ ; in particular, for our models,  $\sigma_{\text{e8}}$  decreases for increasing flattening (see P13 for a comprehensive discussion). Note that  $\sigma_{\text{e8}}$  depends on the line-of-sight direction for non-spherical models; when quoting  $\sigma_{\text{e8}}$  for the latter models, in the following, we refer to the EO projection.

## 2.2 Hydrodynamical equations

The input physics is fully described in DC98 and N14; here, we just summarize the main ingredients. We account for mass sources due to stellar mass losses and SNIa ejecta, momentum injections due to the azimuthal streaming motion of the stellar population and energy sources due to the thermalization of stellar motions and SNIa explosions. Star formation and feedback from a central black hole are not considered. The corresponding equations are

$$\frac{\partial \rho}{\partial t} + \nabla \cdot (\rho \mathbf{u}) = \dot{\rho}_{\text{SN}} + \dot{\rho}_* \equiv \dot{\rho}, \quad (7)$$

$$\rho \frac{\partial \mathbf{u}}{\partial t} + \rho (\mathbf{u} \cdot \nabla) \mathbf{u} = -\nabla p - \rho \nabla \Phi_{\text{tot}} + \dot{\rho} (\mathbf{v} - \mathbf{u}), \quad (8)$$

$$\begin{aligned} \frac{\partial E}{\partial t} + \nabla \cdot (E \mathbf{u}) = & -p \nabla \cdot \mathbf{u} - \mathcal{L} + \dot{\rho}_{\text{SN}} \frac{u_{\text{s}}^2}{2} \\ & + \frac{\dot{\rho}}{2} [\|\mathbf{v} - \mathbf{u}\|^2 + \text{Tr}(\boldsymbol{\sigma}^2)], \end{aligned} \quad (9)$$

where  $\rho$ ,  $\mathbf{u}$ ,  $E$ ,  $p$ ,  $\Phi_{\text{tot}}$ ,  $\mathcal{L}$ ,  $u_{\text{s}}$ ,  $\mathbf{v} = v_{\varphi} \mathbf{e}_{\varphi}$  and  $\boldsymbol{\sigma}^2$  are, respectively, the ISM mass density, velocity, internal energy density, pressure, total gravitational potential, bolometric radiative losses per unit time and volume, the velocity of the SNIa ejecta ( $u_{\text{s}} \simeq 8.5 \times 10^3 \text{ km s}^{-1}$ , corresponding to  $10^{51}$  erg associated with an ejecta of  $1.4 M_{\odot}$ ), the streaming velocity and the velocity-dispersion tensor of the stellar component. The ISM is considered as a fully ionized monoatomic gas, with  $p = (\gamma - 1)E$ ,  $\gamma = 5/3$  and  $\mu \simeq 0.62$ ; as usual, the gas self-gravity is neglected.

The total mass injection rate per unit volume  $\dot{\rho}$  has a contribution from SNIa events  $\dot{\rho}_{\text{SN}} = \alpha_{\text{SN}}(t)\rho_*$  and from stellar winds  $\dot{\rho}_* = \alpha_*(t)\rho_*$ , where

$$\alpha_{\text{SN}}(t) = \frac{1.4 M_{\odot}}{M_*} R_{\text{SN}}(t), \quad \alpha_*(t) = 3.3 \times 10^{-12} t_{12}^{-1.3} (\text{yr}^{-1}). \quad (10)$$

**Table 1.** Fundamental galaxy parameters for the NFW and Einasto sets of models.

Name	$L_B$ ( $10^{11} L_{B\odot}$ )	$R_e$ (kpc)	$M_*$ ( $10^{11} M_\odot$ )	$M_h$ ( $10^{11} M_\odot$ )	$\sigma_{e8}^{\text{NFW}}$ ( $\text{km s}^{-1}$ )	$\sigma_{e8}^{\text{EIN}}$ ( $\text{km s}^{-1}$ )	$f_{\text{DM}}^{\text{NFW}}$	$f_{\text{DM}}^{\text{EIN}}$	$c$
(1)	(2)	(3)	(4)	(5)	(6)	(7)	(8)	(9)	(10)
EO <sup>200</sup>	0.27	4.09	1.25	25	200	200	0.61	0.57	37
EO4 <sup>200</sup> <sub>IS</sub>	0.27	4.09	1.25	25	166	166	0.63	0.59	37
EO4 <sup>200</sup> <sub>VD</sub>	0.27	4.09	1.25	25	179	179	0.63	0.59	37
EO7 <sup>200</sup> <sub>IS</sub>	0.27	4.09	1.25	25	124	124	0.66	0.62	37
EO7 <sup>200</sup> <sub>VD</sub>	0.27	4.09	1.25	25	148	149	0.66	0.62	37
FO4 <sup>200</sup> <sub>IS</sub>	0.27	4.09	1.25	25	178	179	0.59	0.55	37
FO4 <sup>200</sup> <sub>VD</sub>	0.27	4.09	1.25	25	191	192	0.59	0.55	37
FO7 <sup>200</sup> <sub>IS</sub>	0.27	4.09	1.25	25	150	151	0.57	0.53	37
FO7 <sup>200</sup> <sub>VD</sub>	0.27	4.09	1.25	25	178	179	0.57	0.53	37
EO <sup>250</sup>	0.65	7.04	3.35	67	250	250	0.59	0.55	28
EO4 <sup>250</sup> <sub>IS</sub>	0.65	7.04	3.35	67	207	208	0.62	0.57	28
EO4 <sup>250</sup> <sub>VD</sub>	0.65	7.04	3.35	67	223	224	0.62	0.57	28
EO7 <sup>250</sup> <sub>IS</sub>	0.65	7.04	3.35	67	154	155	0.66	0.61	28
EO7 <sup>250</sup> <sub>VD</sub>	0.65	7.04	3.35	67	184	185	0.66	0.61	28
FO4 <sup>250</sup> <sub>IS</sub>	0.65	7.04	3.35	67	223	224	0.57	0.53	28
FO4 <sup>250</sup> <sub>VD</sub>	0.65	7.04	3.35	67	240	241	0.57	0.53	28
FO7 <sup>250</sup> <sub>IS</sub>	0.65	7.04	3.35	67	189	190	0.56	0.51	28
FO7 <sup>250</sup> <sub>VD</sub>	0.65	7.04	3.35	67	223	224	0.56	0.51	28
EO <sup>300</sup>	1.38	11.79	7.80	160	300	300	0.62	0.57	22
EO4 <sup>300</sup> <sub>IS</sub>	1.38	11.79	7.80	160	248	249	0.64	0.60	22
EO4 <sup>300</sup> <sub>VD</sub>	1.38	11.79	7.80	160	267	269	0.64	0.60	22
EO7 <sup>300</sup> <sub>IS</sub>	1.38	11.79	7.80	160	185	185	0.68	0.64	22
EO7 <sup>300</sup> <sub>VD</sub>	1.38	11.79	7.80	160	221	223	0.68	0.64	22
FO4 <sup>300</sup> <sub>IS</sub>	1.38	11.79	7.80	160	266	268	0.60	0.55	22
FO4 <sup>300</sup> <sub>VD</sub>	1.38	11.79	7.80	160	286	288	0.60	0.55	22
FO7 <sup>300</sup> <sub>IS</sub>	1.38	11.79	7.80	160	224	225	0.59	0.54	22
FO7 <sup>300</sup> <sub>VD</sub>	1.38	11.79	7.80	160	265	267	0.59	0.54	22

*Notes:* (1) Model name: E0 identifies the spherical progenitor, and the superscript is the value of  $\sigma_{e8}$ . For the other models, the nomenclature is as follows: for example, FO4<sup>200</sup><sub>IS</sub> means an FO-flattened E4 galaxy, obtained from the EO<sup>200</sup> progenitor, with isotropic rotation. (2) Luminosities in the  $B$  band. (3) Effective radius (for an FO view for FO-built models, and an EO view for EO-built models). For FO-built models, the EO effective radius is reduced by a factor  $\sqrt{q}$  (Section 2.1). (4) Total stellar mass. (5) Total DM mass. (6)–(7) Stellar velocity dispersion, as the luminosity-weighted average within a circular aperture of radius  $R_e/8$ , for the NFW and Einasto sets, respectively; for non-spherical models,  $\sigma_{e8}$  is the EO viewed value. (8)–(9) DM fraction enclosed within a sphere of radius  $R_e$  for the NFW and Einasto sets, respectively. (10) Concentration parameter for the NFW set.

The SNIa explosion rate  $R_{\text{SN}}(t)$  is given by

$$R_{\text{SN}}(t) = 0.16 h^2 \times 10^{-12} L_B t_{12}^{-s} (\text{yr}^{-1}), \quad (11)$$

where  $h = H_0/70 \text{ km s}^{-1} \text{ Mpc}^{-1}$ ,  $L_B$  is the present epoch  $B$ -band galaxy luminosity in blue solar luminosities,  $t_{12}$  is the age of the stellar population in units of 12 Gyr and  $s$  parametrizes the past evolution. The SNIa's heating rate  $L_{\text{SN}}(t)$  is obtained from equation (11) by assuming that each SNIa event releases  $10^{51}$  erg, and we adopt  $s = 1$  in equation (11). Since the volume-integrated energy and mass injections are dominated by  $L_{\text{SN}}$  and stellar mass losses, respectively, this choice of  $s$  produces a secular time-increase of the specific heating  $L_{\text{SN}}/\dot{\rho}$  of the input mass, due to the different time dependence of the mass and energy inputs (e.g. Pellegrini 2012).

The radiative cooling is implemented by adopting a modified version of the cooling law reported in Sazonov et al. (2005), with the lower limit for the ISM temperature of  $T = 10^4$  K (see N14 for more details). We also calculate the X-ray emission in the 0.3–8 keV *Chandra* band, and the X-ray-emission-weighted temperature as

$$L_X = \int \varepsilon_X dV, \quad T_X = \frac{\int T \varepsilon_X dV}{L_X}, \quad (12)$$

respectively, where  $\varepsilon_X$  is the thermal emissivity in the energy range 0.3–8 keV of a hot, collisionally ionized plasma, obtained by the spectral fitting package *xSPEC*<sup>1</sup> (spectral model *APEC*; Smith

<sup>1</sup> <http://heasarc.nasa.gov/xanadu/xspec/>

et al. 2001), and the volume integrals are performed over the whole computational mesh.

As in N14, all the simulations are performed with the ZEUS-MP2 code in cylindrical coordinates, in order to better and uniformly resolve the galaxy equatorial region. The adopted 2D axisymmetric  $(R, z)$  grid is organized in  $480 \times 960$  logarithmically spaced points, extending out to  $\simeq 100$  kpc, with a resolution of  $\simeq 90$  pc in the central 10 kpc. We assume that at the beginning of the simulation each galaxy is 2 Gyr old and is depleted of gas due to the feedback of the stellar population; the evolution is followed for 11 Gyr, until an age of 13 Gyr.

### 2.3 The contribution of stellar kinematics to the ISM energetics

The main issue investigated in this paper is the effect of flattening and ordered rotation on the X-ray luminosity and temperature of the ISM. Analytical studies, based on the global energetic arguments, showed that different and competitive effects should be taken into account (CP96; Pellegrini 2011; P13). Some of the expectations have been confirmed by past numerical studies, even though the galaxy models adopted were not tailored on realistic elliptical galaxies, but more on S0/Sa (DC98; N14). In any case, such studies showed that different physical phenomena can be important as a function of the galaxy mass and potential well depth (i.e. whether the ISM is outflowing or inflowing).

In order to compare the results of the numerical simulations with the global energetic estimates, the following quantities are also computed by the hydrodynamical code. The first is the thermalization of stellar random motions, providing an energy input per unit time to the ISM of

$$L_\sigma \equiv \frac{1}{2} \int \dot{\rho} \text{Tr}(\sigma^2) dV. \quad (13)$$

Note that while the contribution from stellar random motions is fully independent of the ISM velocity field (see equation 8), the thermalization of the stellar ordered (streaming) motion depends on the relative motion between stars ( $\mathbf{v}$ ) and ISM ( $\mathbf{u}$ ),

$$\begin{aligned} L_v &\equiv \frac{1}{2} \int \dot{\rho} \|\mathbf{v} - \mathbf{u}\|^2 dV \\ &= \frac{1}{2} \int \dot{\rho} (u_R^2 + u_z^2) dV + \frac{1}{2} \int \dot{\rho} (v_\varphi - u_\varphi)^2 dV = L_m + L_\varphi, \end{aligned} \quad (14)$$

so that, at variance with  $L_\sigma$ , it cannot be predicted a priori from the knowledge of the galaxy structure and kinematics. Note that in our galaxy models  $\mathbf{v} = v_\varphi \mathbf{e}_\varphi$ , and  $L_m$  and  $L_\varphi$  are, respectively, the energy input rate due to the ISM velocity in the meridional plane  $(R, z)$ , and to the relative velocity of stars and the ISM in the azimuthal direction.

As in P13 and N14, we parametrize the thermalized fraction of the available kinetic energy due to stellar streaming with

$$\gamma_{\text{th}} \equiv \frac{L_v}{L_{\text{rot}}}, \quad (15)$$

where

$$L_{\text{rot}} \equiv \frac{1}{2} \int \dot{\rho} \|\mathbf{v}\|^2 dV \quad (16)$$

is the energy input per unit time that would be injected in a galaxy with an ISM at rest (i.e.  $\mathbf{u} = 0$ ), due to thermalization stellar streaming motions. Note that  $\gamma_{\text{th}}$  is undefined (formally, it diverges) for

VD-supported models, and can be very large for slow rotators and/or for gas flows with large velocities in the meridional plane (as in the case of galactic winds). Using these definitions, the total energy supplied to the ISM due to stellar motions can be written as

$$L_{\text{kin}} \equiv L_\sigma + L_v = L_\sigma + \gamma_{\text{th}} L_{\text{rot}}. \quad (17)$$

Finally, all the luminosities defined above can be converted into equivalent temperatures as

$$T_\sigma = \frac{\mu m_p}{3k_B M_*} \int \rho_* \text{Tr}(\sigma^2) dV, \quad T_{\text{rot}} = \frac{\mu m_p}{3k_B M_*} \int \rho_* \|\mathbf{v}\|^2 dV, \quad (18)$$

where  $k_B$  is the Boltzmann constant and  $m_p$  is the proton mass so that

$$T_{\text{kin}} = T_\sigma + \gamma_{\text{th}} T_{\text{rot}}; \quad \gamma_{\text{th}} T_{\text{rot}} = T_m + T_\varphi. \quad (19)$$

## 3 RESULTS

Here, we present the main results of the simulations, focusing on the hydrodynamical evolution of a few representative models, and then on the global properties  $L_X$  and  $T_X$  for the two sets of models.

### 3.1 Hydrodynamics

For illustrative purpose, we present the hydrodynamical evolution of some selected EO-built models belonging to the NFW set. In particular, in the family derived from the E0 progenitor with  $\sigma_{\text{e8}} = 250 \text{ km s}^{-1}$  (Section 3.1.1), we consider the velocity-dispersion-supported E7 model (Section 3.1.2), and the corresponding E7 isotropic rotator (Section 3.1.3). In Section 3.1.4, we summarize the main similarities and differences with the other models, as well as some considerations on the behaviour of the thermalization parameter  $\gamma_{\text{th}}$ .

In general, as found in N14, the gas flows are found to evolve through two well-defined hydrodynamical phases. At the beginning, all the ISM quantities (density, internal energy and velocity) are nearly symmetric with respect to the galactic equatorial plane. During the evolution, the velocity fields become more and more structured, until, after a certain time that depends on the specific model, the reflection symmetry is lost, and it is never restored.

#### 3.1.1 The E0<sup>250</sup> progenitor

The initial ( $t = 2.4$  Gyr) and final ( $t = 13$  Gyr) configurations of the ISM are shown in Fig. 1, where we show the meridional section of the ISM temperature (top panels), and the ratio of the heating and cooling time  $t_{\text{heat}}/t_{\text{cool}}$  (bottom panels; green corresponds to a cooling-dominated region while purple refers to a heating region). The arrows show the meridional velocity field.

All the ISM physical quantities are stratified on a spherical shape, as a consequence of the galaxy spherical symmetry. A decoupled flow is soon established ( $t \simeq 2.4$  Gyr), with an inflow in a round central region surrounded by an outflowing atmosphere. At the same time, cold gas accumulates into the centre, due to the lack of rotational support. Starting from the time of decoupling, the evolution appears to be nearly stationary.

The evolution of the ISM temperature reflects the flow evolution: a hot atmosphere approximately isothermal ( $T \simeq 5 \times 10^6$  K) forms at the beginning, containing a cooling region of radius  $\simeq 5$  kpc that leads to the formation of a cold core at the very centre (see the

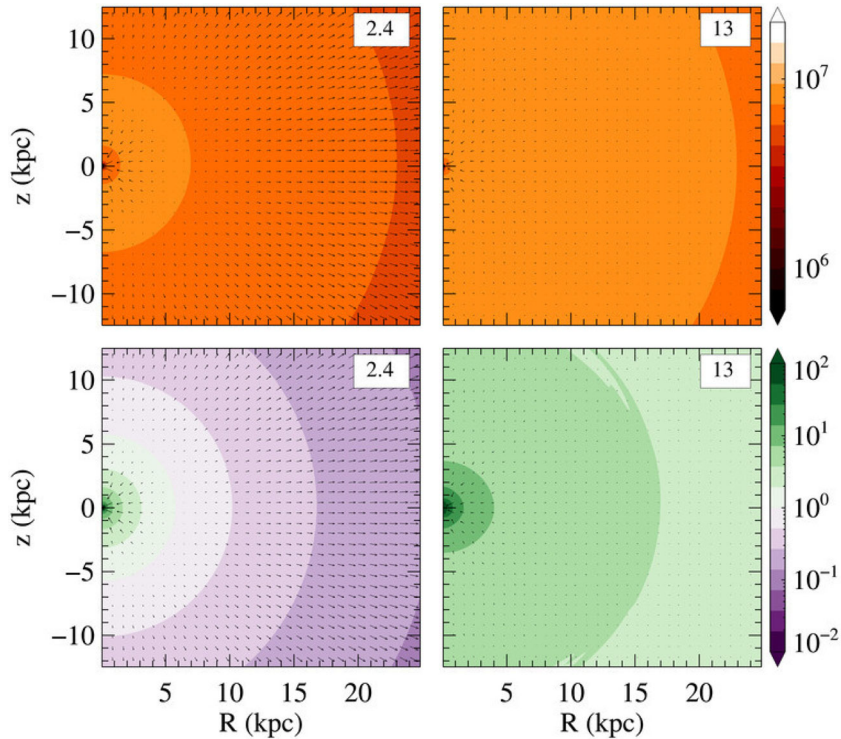


**Figure 1.** Meridional section of temperature (in K, top panels) and heating over cooling time ratio  $t_{\text{heat}}/t_{\text{cool}}$  (bottom panels), for the  $\text{E0}^{250}$  model with NFW halo (Table 1), at the times specified in the boxes (in Gyr). We define  $t_{\text{cool}} = E/\mathcal{L}$  and  $t_{\text{heat}}$  as the ratio between  $E$  and the source terms in the r.h.s of equation (9). In the bottom plots, green regions refer to cooling gas, while purple indicate heating-dominated regions, as indicated by the colour scale. Arrows show the meridional velocity field, with the longest arrows corresponding to  $127 \text{ km s}^{-1}$ .

green region in the bottom panels). At the end of the simulation, a total of  $\simeq 2.6 \times 10^{10} M_{\odot}$  of gas is cooled at the centre, while  $\simeq 5 \times 10^9 M_{\odot}$  has been ejected as a galactic outflow. Overall,  $L_X$  and  $T_X$  of this model do not present significant fluctuations (Fig. 2, solid green line), with  $L_X$  steadily decreasing and  $T_X$  steadily increasing in pace with the time evolution of mass sources and specific heating.

### 3.1.2 The $\text{EO7}_{\text{VD}}^{250}$ galaxy

The ISM evolution of the velocity-dispersion-supported  $\text{EO7}_{\text{VD}}^{250}$  model presents important similarities with the spherical progenitor. This is not surprising, due to the absence of angular momentum, and to the fact that in general the gravitational potential is much rounder than the associated stellar density distribution (in addition, recall that the DM halo is kept spherical). Therefore, the only major differences between the  $\text{E0}^{250}$  progenitor and the  $\text{EO7}_{\text{VD}}^{250}$  model are the different spatial regions where the gas is injected, and the different velocity-dispersion field of the stars. A direct comparison of the evolution of the two models can be obtained by inspection of Fig. 3, analogous of Fig. 1. At early times, the flow is kinematically decoupled, with an equatorial outflow due to the concentrated heating on the equatorial plane (purple region), associated with a polar accretion along the  $z$ -axis, evidenced by the green cooling region. As in the spherical progenitor, due to the lack of centrifugal support, the cooling material falls directly towards the galaxy centre, where a dense, cold core is formed during the first hundred Myr. The early flow evolution is characterized by equatorial symmetry and large-scale meridional vortices. The symmetry is lost at  $t \simeq 3 \text{ Gyr}$ , followed by a secular decrease of the velocity field.

The flow velocities are larger than in the  $\text{E0}$  progenitor, due to the weaker gravitational field (consequence of the  $\text{EO}$  flattening). The evolution of  $L_X$  and  $T_X$  are shown in Fig. 2 (black solid line). Compared to the  $\text{E0}$  progenitor, the  $\text{EO7}_{\text{VD}}^{250}$  model has a fainter  $L_X$  and a lower  $T_X$ , but a similar lack of significant fluctuations in  $L_X$  and  $T_X$ . At the end of the simulation, the cooled gas at the centre for this model is  $\simeq 1.8 \times 10^{10} M_{\odot}$ , while the ejected ISM is  $\simeq 7 \times 10^9 M_{\odot}$ . If this model is allowed to have the accretion physics activated for the central black hole, we expect to recover the complex AGN feedback phenomena described elsewhere (Ciotti & Ostriker 2012), with significant reduction of the central accreted mass.

### 3.1.3 The $\text{EO7}_{\text{IS}}^{250}$ galaxy

Previous explorations (DC98; N14) revealed that the evolution of gas flows in galaxies with significant ordered rotation of the stellar component is more complex than in velocity-dispersion-supported systems of similar structure. This is confirmed by the present study. The flow evolution of the  $\text{EO7}_{\text{IS}}^{250}$  is shown in Fig. 4 (where more panels than the previous two models are shown, to better illustrate the more structured evolution of the ISM).

The first major difference of the present model with respect to its VD counterpart is the formation, due to angular momentum conservation, of a rotationally supported, thin and dense cold disc, with a size of  $\simeq 5 \text{ kpc}$ . The cold disc grows during galaxy evolution, reaching a final size of  $\simeq 10 \text{ kpc}$ . A hot and rarefied zone that secularly increases in size surrounds the cold disc. At early times ( $t \simeq 2.1 \text{ Gyr}$ ), the ISM in the central regions cools and collapses, producing a low-density region that cannot be replenished by the inflowing gas, which is supported by angular momentum. As time

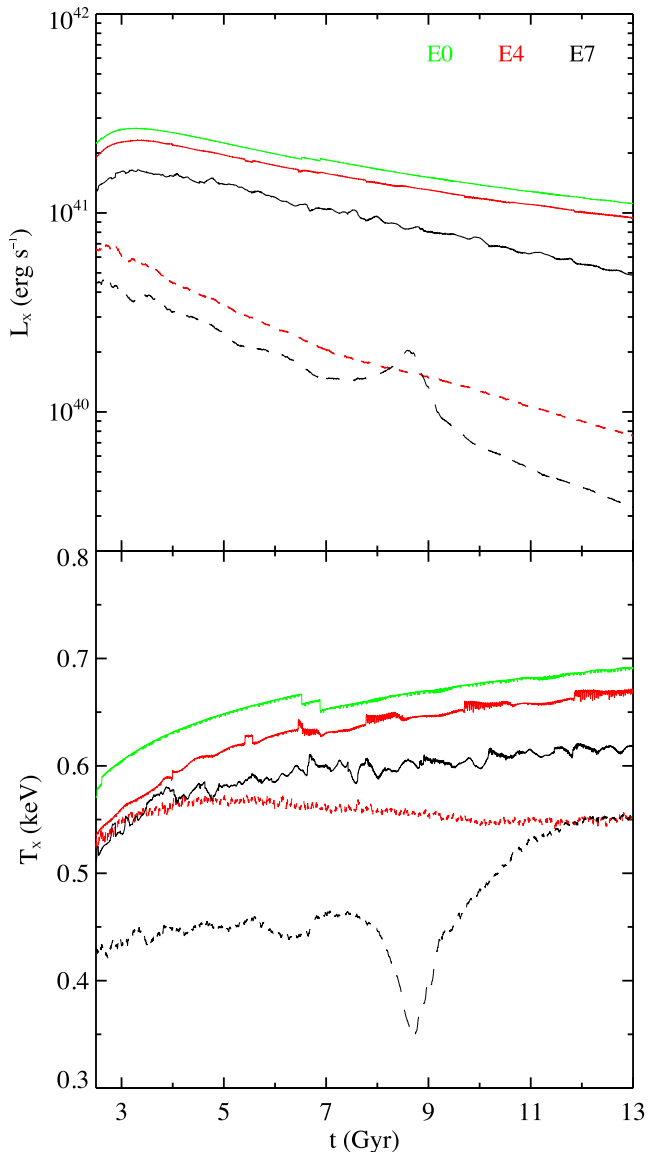


**Figure 2.** Time evolution of the X-ray luminosity  $L_X$  and X-ray-emission-weighted temperature  $T_X$  for the family derived from the  $E0^{250}$  model with the NFW halo. The red and black lines report the evolution of the VD models (solid) and of the IS models (dashed). The colours map the flattening: green, red and black correspond to the E0, E4 and E7 galaxies, respectively.

increases, the combination of the centrifugal barrier, which keeps the centre at low density, and the secular increase of the specific heating produces the growth of the heating region (purple zone in Fig. 4, roughly extending as the cold thin disc). We stress that the time and spatial evolution of the  $t_{\text{heat}}/t_{\text{cool}}$  ratio is more affected by cooling time variations than by the secular decrease of the heating time. Being the cooling time very sensitive to the ISM density,  $t_{\text{heat}}/t_{\text{cool}}$  is strongly related to the density distribution evolution.

Another important difference between  $EO7_{\text{IS}}^{250}$  and  $EO7_{\text{VD}}^{250}$  concerns the ISM kinematics outside the equatorial plane. As is apparent in Fig. 4, starting from  $t \simeq 8$  Gyr, the meridional velocity field develops a very complex pattern of vortices above and below the equatorial plane. This behaviour is associated with the formation of a large cooling region (in green), and corresponds, respectively, to a peak and a drop in the evolution of  $L_X$  and  $T_X$  (Fig. 2, black dashed line). Note also that  $L_X$  and  $T_X$  are the lowest of the three models

$EO^{250}$ ,  $EO7_{\text{VD}}^{250}$  and  $EO7_{\text{IS}}^{250}$ . The cold mass accreted at the centre is now much smaller ( $\simeq 2.9 \times 10^3 M_{\odot}$ ), while the mass in the cold disc is  $\simeq 1.5 \times 10^{10} M_{\odot}$ , and the mass ejected in the galactic wind is  $\simeq 1.1 \times 10^{10} M_{\odot}$ . Note that a central black hole in this rotating model would produce a significantly weaker AGN activity than in the  $EO7_{\text{VD}}^{250}$  model.

Even if the models are structurally quite different from the S0/Sa models in N14, they show a similar ISM evolution, with a lower  $L_X$  and  $T_X$  in rotating models. However, the number of oscillations in the present set of models is much lower.

### 3.1.4 The thermalization parameter and an overview of all models

A useful global parameter that helps to quantify the heating of the ISM due to stellar ordered motions is the thermalization parameter  $\gamma_{\text{th}}$  (Section 2.3; P13; N14). For the  $EO7_{\text{IS}}^{250}$  galaxy, we found that  $\gamma_{\text{th}}$  remains at low values ( $\simeq 0.08$ – $0.28$ , see Tables A1 and A2) over the evolution; this means that (1) the ISM almost corotates with the stellar population everywhere, and (2) there are not significant ISM velocities in the meridional plane. Note that  $\gamma_{\text{th}}$  can attain large values, even larger than unity (see the examples described later in this section). This happens in general in low-rotation, low-mass systems, where  $\gamma_{\text{th}}$  is fully dominated by high-velocity galactic winds (see equation 14), so that  $L_{\text{m}}$  is large even though  $L_{\varphi}$  remains low. Remarkably enough, also in these high- $\gamma_{\text{th}}$  cases, the azimuthal thermalization parameter  $\gamma_{\text{th}}^{\varphi} \equiv L_{\varphi}/L_{\text{rot}}$  (equation 14) remains low (see Tables A1 and A2), indicating that the ISM rotates almost as fast as the stellar population. One could be tempted to interpret the lack of thermalization of a significant fraction of ordered motions in all the IS models as the reason for the lower  $T_X$  of the IS models with respect to their VD counterparts (Fig. 2, black and red dashed lines versus the solid lines). However, even if this effect certainly contributes, it is not the main reason for the lower  $T_X$  in rotating models. Indeed, we found that artificially adding the ‘missing’ thermalization to the equations of hydrodynamics in dedicated test simulations of rotating models leads only to a negligible increase in  $T_X$  (see also N14), showing that also other effects contribute to the low  $T_X$  (see Section 3.3).

We now discuss similarities and differences of the hydrodynamical evolution in galaxy models of different mass (i.e. derived from progenitors with different  $\sigma_{\text{e8}}$ ). The main features of the family with the spherical progenitor of  $\sigma_{\text{e8}} = 250 \text{ km s}^{-1}$  are maintained in the  $\sigma_{\text{e8}} = 300 \text{ km s}^{-1}$  family. In particular, independently of the DM halo profile, increasing  $\sigma_{\text{e8}}$ , both  $L_X$  and  $T_X$  increase. This is expected because more massive models can retain more and hotter gas independently of the flattening and kinematical support. In more massive models, the  $L_X$  and  $T_X$  are less fluctuating with time, the outflow velocities of the galaxy outskirts are lower, and the complicated meridional circulation in the rotating models is reduced (as also found by N14). The final properties of all models are given in Tables A1 and A2. A full discussion of  $L_X$  and  $T_X$  is given in Sections 3.2 and 3.3. In general, the ISM temperature, luminosity, radius of the central cooling region and inflow velocity are directly proportional to  $\sigma_{\text{e8}}$ . In massive ( $\sigma_{\text{e8}} \geq 250 \text{ km s}^{-1}$ ) models, at fixed galaxy mass, pure flattening does not affect significantly  $L_X$  and  $T_X$ , while a major reduction in  $L_X$  and  $T_X$  is obtained for the isotropic rotators.

The situation is quite different for the families with low-mass progenitors ( $\sigma_{\text{e8}} = 200 \text{ km s}^{-1}$ ). These are the only cases where a transition to a global wind can be induced by a change of shape or by rotation, in accordance with the energetic analysis of CP96.

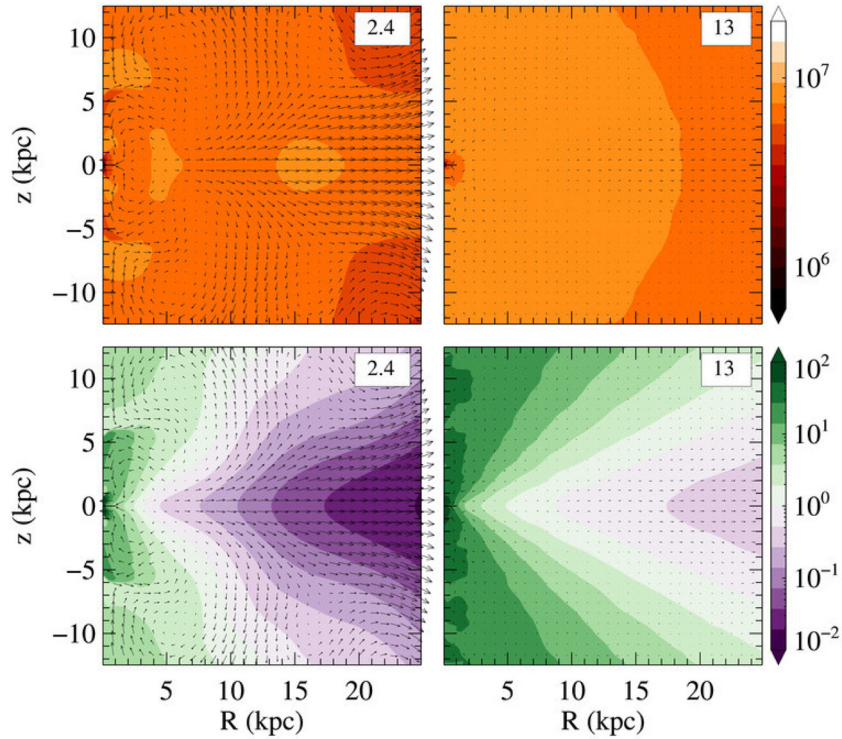


**Figure 3.** Meridional sections of the temperature (top panels) and heating over cooling time ratio (bottom panels) for the EO7<sub>VD</sub><sup>250</sup> model of the NFW set, at the times specified in the boxes (in Gyr). Arrows are normalized to the same velocity as in Fig. 1.

This is especially true for the less concentrated Einasto models. In these global wind cases,  $L_X$  drops to very low values, due to the very low ISM density, and  $T_X$  keeps larger than expected from the trend defined by non-wind models (see Section 3.3), due to the reduced cooling, and to thermalization of the meridional motions (see Sections 3.2 and 3.3 for a detailed discussion). The sensitivity of the flow phase for low-mass models near the transition to the outflow is shown for example by the EO7<sub>VD</sub><sup>200</sup> model with the NFW halo, which experiences two quite distinct evolutionary phases (Fig. 5). At the beginning, a significant equatorial degassing is apparent, coincident with the strong heating in that region. As time increases, the velocity field in the outflow region decreases and gas cooling becomes more and more important outside the V-shaped region around the equator. However, after  $\simeq 9$  Gyr, the secular increase of the specific heating, coupled with the shallow potential well, induces again higher and higher velocities. The gas temperature increases again while  $L_X$  decreases. The associated EO7<sub>IS</sub><sup>200</sup> model is in a permanent wind phase from the beginning, thus showing the additional effect of rotation in flattened, low-mass galaxies. The differences between the EO7<sub>VD</sub><sup>200</sup> and EO7<sub>IS</sub><sup>200</sup> models are quantified by the associated values of the global quantities at the end of the simulation (see Table A1):  $M_{\text{hot}} = 0.66 \times 10^9 M_\odot$  and  $0.24 \times 10^9 M_\odot$  in the VD and IS cases, respectively, where  $M_{\text{hot}}$  is the ISM mass having  $T > 10^6$  K. Little accretion at the centre is present in the VD but not in the IS, and this shows how different AGN activity may be expected in rotating versus non-rotating galaxies, also at low galaxy masses.

### 3.2 The X-ray ISM luminosity $L_X$

We now move to describe the properties of  $L_X$  for the whole set of galaxy models, as they would be observed at an age of 13 Gyr. The results are summarized in Fig. 6, where the top panels refer to

the NFW set and the bottom panels to the Einasto set.  $L_X$  is shown versus three different galaxy properties, i.e.  $\sigma_{e8}$  (left-hand panels),  $M_{\text{hot}}$  (central panels) and  $L_B$  (right-hand panels). Remarkably, the range of  $L_X$  values spanned by the models matches the observed one (see for example the observed  $L_X-L_K$  and  $L_X-\sigma_{e8}$  trends in Figs 2 and 5 in Boroson et al. 2011). The most interesting feature of Fig. 6 is the clear  $L_X$  difference between flattened rotating models and models of similar  $\sigma_{e8}$  but velocity dispersion supported. As described in the previous section, the hydrodynamical simulations show that the underluminosity of rotating galaxies with medium to large  $\sigma_{e8}$  is due to a different flow evolution driven by the presence of angular momentum, which prevents the gas from accumulating in the central regions, leading to the creation of a very hot, low-density atmosphere in the centre, and eventually resulting in a lower total  $L_X$ . Instead, in VD models, the ISM flows directly towards the central galactic regions, where a steep density profile is created. This difference in the hot gas density distribution is a major reason for the systematic difference of  $L_X$  (see also Fig. 7). It nicely explains the lower  $L_X$  observed for fast rotators than for slow rotators in the ATLAS sample (Sarzi et al. 2013). ETGs with the lowest  $\sigma_{e8}$  behave differently (see below).

In the central panels of Fig. 6,  $L_X$  is plotted against the hot gas content  $M_{\text{hot}}$ ; each rotating model is shifted to the left of the corresponding VD model; thus, IS models have also a lower  $M_{\text{hot}}$  than VD models. This is due to the presence of recurrent cooling episodes driven by rotation, which further contribute to the lowering of  $L_X$ . With the exception of the models with the lowest  $L_B$ , the systematic differences in  $M_{\text{hot}}$  are not due to escaping ISM (Fig. 8).

Finally, the right-hand panels of Fig. 6 show how  $L_X$  on average increases with the galaxy optical luminosity, however presenting at each  $L_B$  a significant spread in  $L_X$ , consistent with observations (Boroson et al. 2011). At fixed  $L_B$ , round progenitors are found at

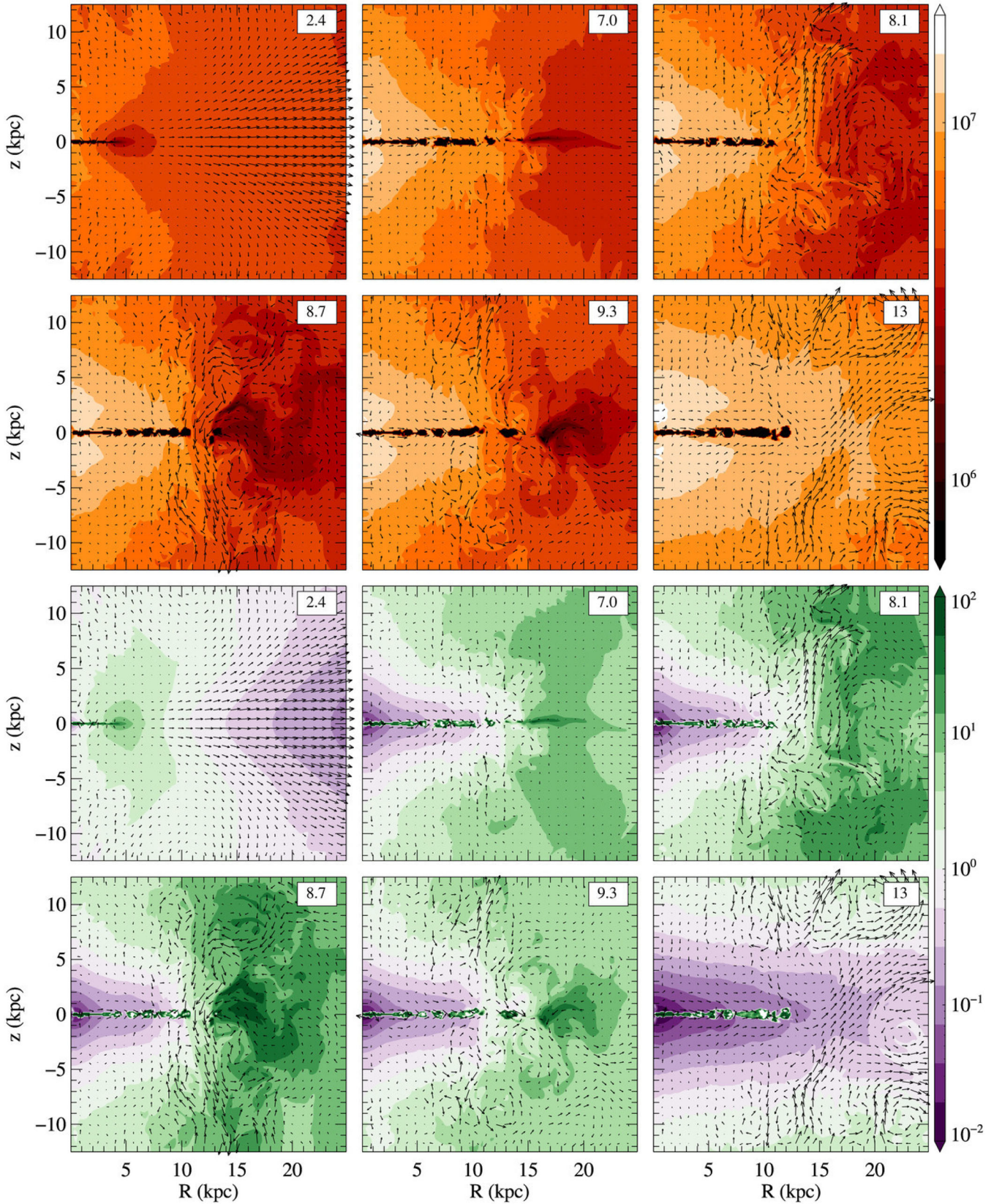


**Figure 4.** Meridional sections of the temperature in K (six top panels) and heating over cooling time ratio (six bottom panels) for the  $EO7_{IS}^{250}$  model of the NFW set, at the times specified in the boxes (in Gyr). Arrows are normalized to the same velocity as in Fig. 1.

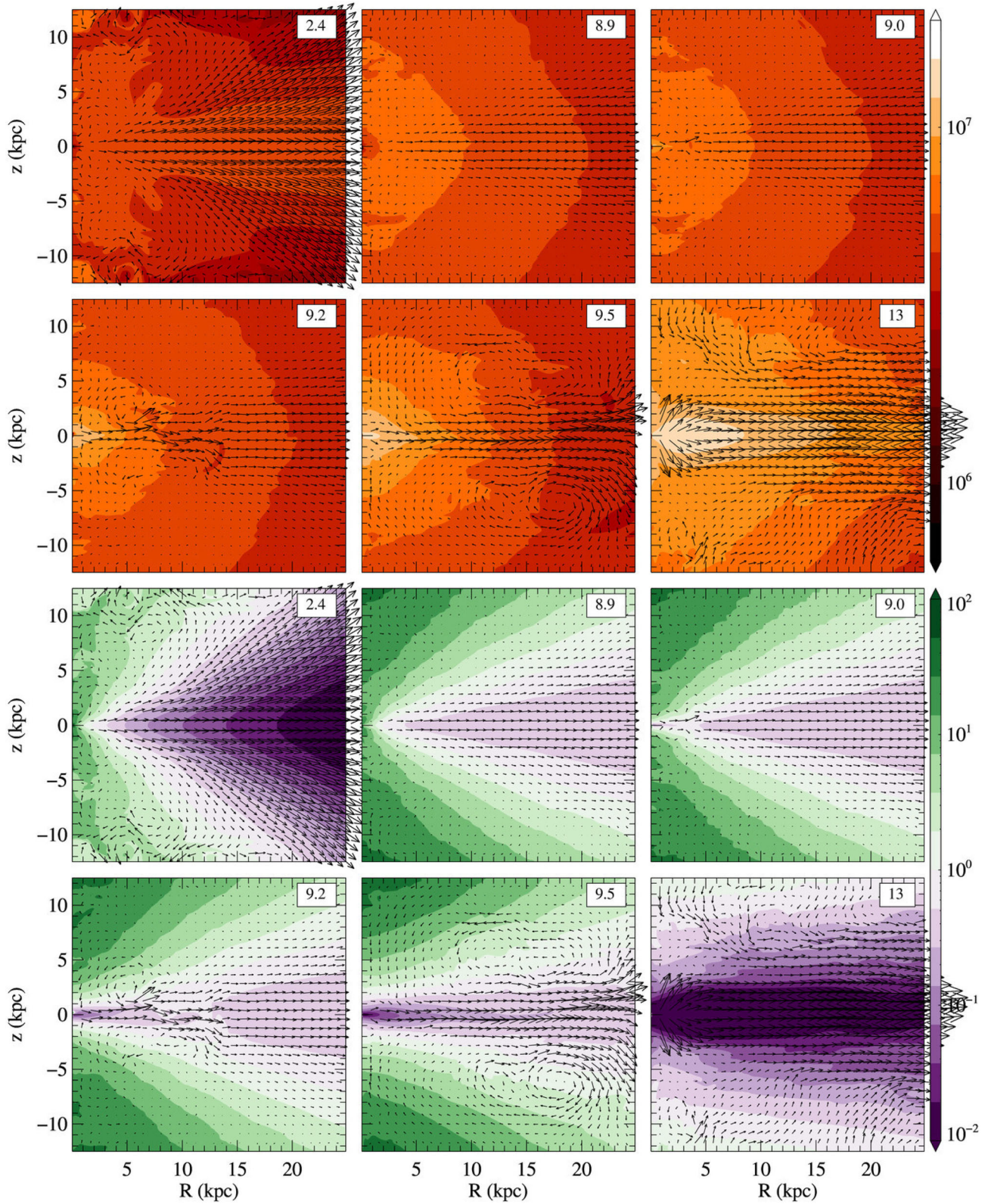


**Figure 5.** Meridional sections of the temperature in K (six top panels) and heating over cooling time ratio (six bottom panels) for the low-mass  $\text{EO7}_{\text{VD}}^{200}$  model of the NFW set, at the times specified in the boxes (in Gyr). Arrows are normalized to the same velocity as in Fig. 1. Note the strong equatorial degassing established at late times.

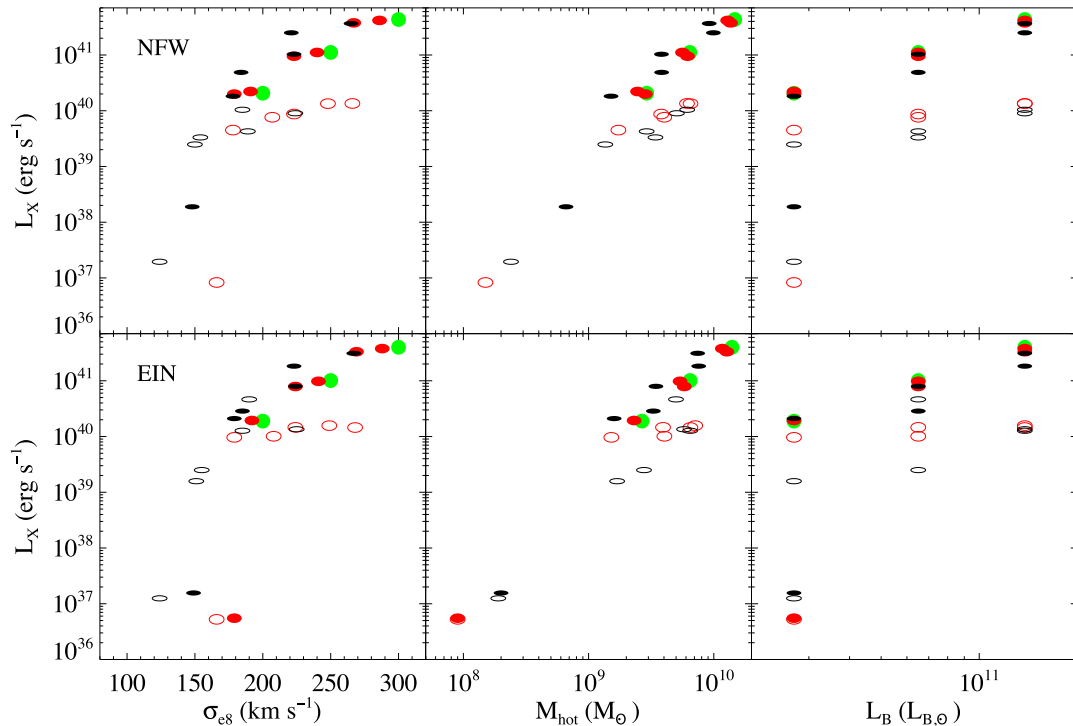


**Figure 6.** ISM X-ray luminosity  $L_X$  in the 0.3–8 keV band at 13 Gyr for all models in the NFW (top panels) and in the Einasto (bottom panels) sets, as a function of  $\sigma_{e8}$ , of the hot ( $T > 10^6$  K) ISM mass and of the galaxy blue optical luminosity; spherical progenitors (green circles) with  $\sigma_{e8} = (200, 250, 300)$  have been considered. The green, red and black colours refer to the E0, E4 and E7 models, respectively. Filled and open symbols indicate the fully velocity-dispersion supported VD models, and the isotropic rotators IS models, respectively.

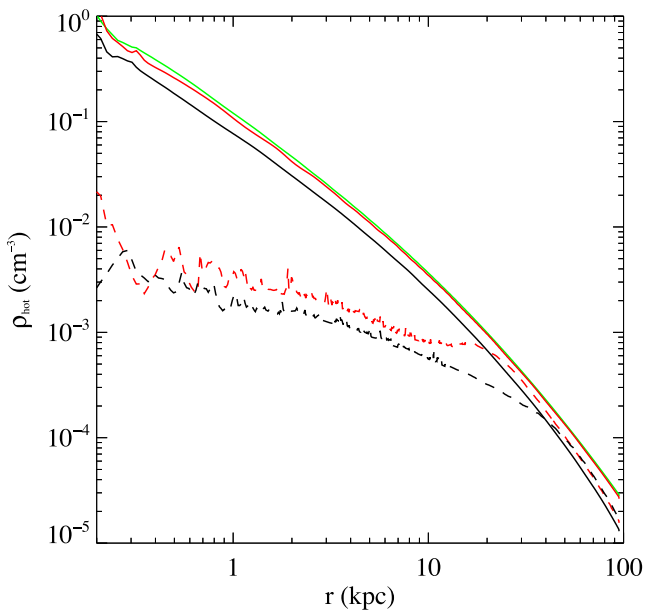


**Figure 7.** Angle-averaged profile of the hot ISM density at  $t = 13$  Gyr for the same models as in Fig. 2. Solid lines refer to VD models, dashed lines refer to IS models.

high  $L_X$ , while the dispersion is associated with a mix of flattening and rotation effects. At each  $L_B$ ,  $L_X$  of the VD models is higher than that of IS ones by up to a factor of  $\simeq 40$ . The largest difference occurs for the more massive and flatter models, and it is much larger than the  $L_X$  variation between a spherical progenitor and its most

flattened VD version. Indeed,  $L_X$  of VD models of identical  $L_B$  with different flattening lies in a narrow range, with a weak trend for the X-ray luminosity to increase as the galaxy model gets rounder. The same behaviour occurs also among IS models with the same  $L_B$ . This indicates that, at fixed  $L_B$  and fixed internal kinematics,  $L_X$  is only marginally sensitive to even large variations of the flattening degree of the stellar component.

A ‘zoom’ on the specific effects of flattening and rotation is given in Fig. 9, where we plot, separately for each  $\sigma_{e8}$ , and for FO and EO built families, the  $L_X$  values of Fig. 6. All models in a given column are characterized by the same optical luminosity. As expected,  $L_X$  of FO subfamilies spans a narrower range of values than that of the EO cases, due to the FO flattening procedure in which the galaxy becomes more concentrated and so outflows are less favoured.

Fig. 9 clearly shows how the models with the  $\sigma_{e8} = 200 \text{ km s}^{-1}$  progenitor behave differently from the rest of the models; this is more evident for the EO flattening, when the galaxy potential well becomes shallower, and thus energetic effects of flattening and rotation are larger than for the FO flattening. For example, the EO7<sub>VD</sub><sup>200</sup> model drops to low  $L_X$ , at variance with the FO7<sub>VD</sub><sup>200</sup> model; this drop happens also for the Einasto EO4<sub>VD</sub><sup>200</sup> model. This sharp  $L_X$  difference is due to the fact that flattening produces a flow transition to a global wind, in accordance with the CP96 analysis, as described in Section 3.1.4. In the NFW case, a further reduction in  $L_X$  is attained when introducing rotation in the EO7<sub>IS</sub><sup>200</sup> model, again in accordance with CP96 and P13, where thermalization of ordered motions does not take place. Note how a transition to a very low  $L_X$  value is also obtained for the NFW EO4<sub>IS</sub><sup>200</sup> model, just by adding rotation. These findings point out the high sensitivity of the flow phase to (even small) changes in the mass profile (e.g. flattening or mass concentration) and in the stellar kinematics (e.g. rotation) at low

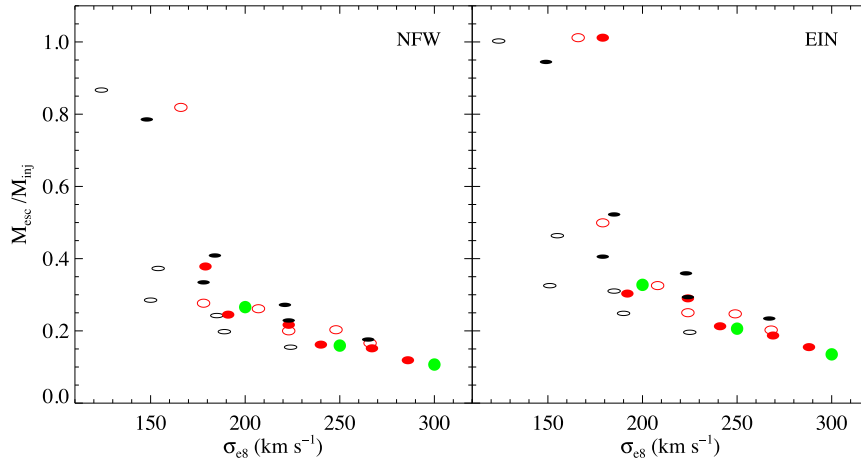


**Figure 8.** Fraction of escaped ISM mass ( $M_{\text{esc}}$ ) with respect to the total injected mass ( $M_{\text{inj}}$ , see Tables A1 and A2) at  $t = 13$  Gyr, as a function of  $\sigma_{e8}$ , for the whole NFW and Einasto sets. The notation for the symbols is the same as in Fig. 6.

galactic masses, for which then it is difficult to predict systematic trends in  $L_X$ . We stress that the VD and IS models in each panel are characterized, by construction, by the same gravitational potential, so that the difference in  $L_X$  is only due to galactic rotation.

### 3.3 The X-ray-emission-weighted temperature $T_X$

The second important diagnostic explored is the 0.3–8 keV luminosity-weighted ISM temperature  $T_X$ . The distribution of the  $T_X$  values for the whole set of models at the end of the simulations is given in Fig. 10, as a function of  $\sigma_{e8}$ ,  $M_{\text{hot}}$  and  $L_B$ .

In general  $T_X$  increases with  $\sigma_{e8}$ , a natural consequence of the deeper potential well associated with larger  $\sigma_{e8}$ . This leads to faster stellar (random and ordered) velocities, with the consequent larger energy input from thermalization of the stellar motions. In addition, in a deeper potential the hot gas is retained at a larger  $T_X$ . The temperature range spanned by the models agrees well with that of real ETGs, and the observed trend of  $T_X$  with  $\sigma_{e8}$  is reproduced (e.g. see fig. 6 in Boroson et al. 2011, who measured  $T_X$  of the pure gaseous component for a sample of 30 ETGs). At high  $\sigma_{e8}$ , the observed  $T_X$  values span a narrower range than in our models, likely because the models include very flat and highly rotating ETGs that are missing in the observed sample. Interestingly, instead, the low- $\sigma_{e8}$  end of the observed  $T_X$ – $\sigma_{e8}$  relation shows an increase of dispersion in the  $T_X$  values, and a hint for a flattening of the relation with respect to the trend shown at larger  $\sigma_{e8}$ . These features are shown also by our models: at low  $\sigma_{e8}$ , the trend of  $T_X$  flattens for NFW models, and the scatter around it increases considerably for the Einasto models. This is explained as the temperature counterpart of the  $L_X$  behaviour at low  $\sigma_{e8}$  in Fig. 6: the transition to global winds in flattened and rotating low-mass galaxies leads to a reduction in  $L_X$  and an increase of  $T_X$  with respect to the trend defined by more massive ETGs, or ETGs of similar mass but not in wind. The change in the relationship is due to the thermalization of the resulting meridional flows (while the thermalization of galaxy rotation remains negligible), and to the lower cooling (see Section 3.1.4). For example, the EO4<sub>VD</sub><sup>200</sup> and EO4<sub>IS</sub><sup>200</sup> models in the Einasto set have high  $T_X$  as a consequence of the transition to the wind phase.

The middle panels of Fig. 10 show the  $T_X$  distribution as a function of  $M_{\text{hot}}$ . In the NFW set, there is a sequence of  $T_X$  values clearly visible at  $M_{\text{hot}} > 2 \times 10^9 M_\odot$ , with VD models hotter than the

corresponding IS models. However, the three models with the smallest amount of hot ISM ( $M_{\text{hot}} < 10^9 M_\odot$ ) have higher temperatures than one would expect extrapolating the  $T_X$  sequence to very low values of  $M_{\text{hot}}$ , as a consequence of the transition to the wind phase. A change in the trend is even more visible in the low-mass Einasto models, where the stronger tendency to establish a global wind leads to an increase of  $T_X$  at very low  $M_{\text{hot}}$ , reaching values even higher than in VD models with large X-ray haloes. In conclusion, at medium- to high- $\sigma_{e8}$ ,  $T_X$  of VD models tends to remain above that of rotating models; at low  $\sigma_{e8}$ , in addition to the cooler branch of rotating models, another hotter branch of IS and VD models appears, made by models in wind.

Finally, the right-hand panels of Fig. 10 show again how  $T_X$  of IS models is systematically lower with respect to that of VD ones of same  $L_B$ , with the exception of those in the wind phase. As for  $L_X$ ,  $T_X$  of VD models is dominated by the dense central luminous regions. In IS models, instead, the central region is hotter than in VD models, but it is also at a lower density, so that its contribution to  $T_X$  is marginal, and  $T_X$  is more affected by colder ( $T \simeq 2 \times 10^6$  K) gas located in the outer regions. Thus, the main reason of the lower  $T_X$  in IS models of medium–high mass is not galaxy shape, but the importance of galaxy rotation, which drives the hydrodynamical evolution (Section 3.1.3). From the Jeans equations, the more a galaxy is flat, the more it can be rotating; thus, the E7 IS models are cooler than their VD counterparts, and by a larger amount than for the analogous E4 pair, due to the stronger rotation in the E7 models.

The trend of  $L_X$  with  $T_X$  for all models is shown in the lower panels of Fig. 11. Also, in this figure, the models behaviour is strikingly similar to that observed in the Boroson et al. (2011) sample, where a narrow correlation at high  $T_X \gtrsim 0.5$  keV is broken into an almost vertical band of  $L_X$  values spanning a large range (from  $10^{38}$  to  $10^{41}$  erg s<sup>−1</sup>) for  $kT$  covering a small range (from 0.2 to 0.5 keV). This trend in the models is explained as the product of the effects described above, resulting in a high sensitivity of the flow phase to small variations in the galaxy structure at the lowest galaxy masses, which on average also have  $T_X < 0.5$  keV.

In analogy with Fig. 9, in Fig. 12, we show the distribution of  $T_X$  of all models, as a function of  $\sigma_{e8}$  and of the flattening procedure. The additional symbols (crosses) represent  $T_\sigma$  (see equation 18); thus, they give the temperatures associated with the thermalization of all stellar velocities for VD models (filled crosses), and only

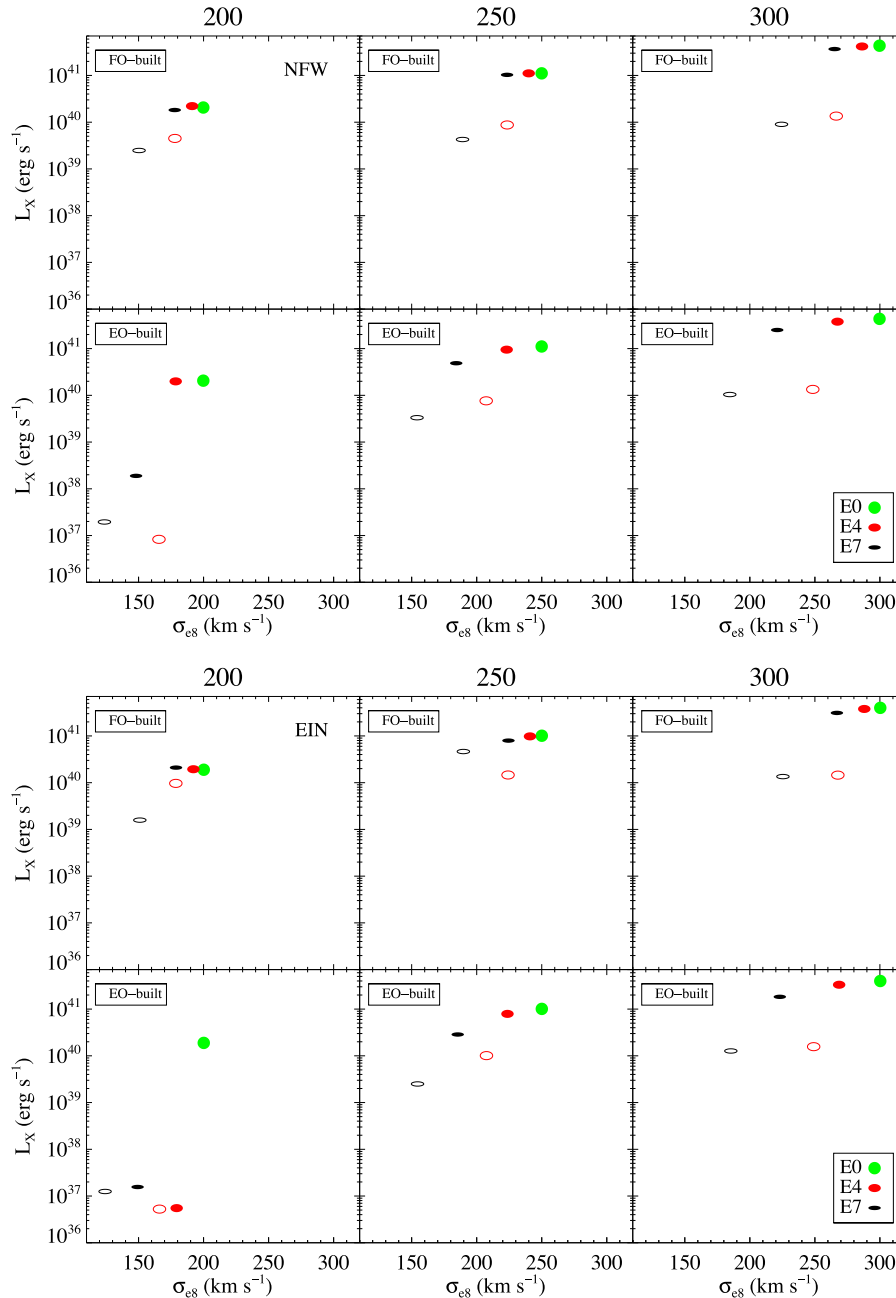


**Figure 9.** ISM X-ray luminosity  $L_X$  in the 0.3–8 keV band at 13 Gyr for the models in the NFW (top six panels) and in the Einasto (bottom six panels) sets as a function of  $\sigma_{e8}$ . Different columns show the results for the families obtained from the spherical progenitors with  $\sigma_{e8} = (200, 250, 300)$  km s $^{-1}$ , and refer to model flattened according to the EO or FO procedure.

to the random part of the stellar velocities for IS models (open crosses). The values of  $T_\sigma$  depend only on the galaxy structure, and do not contain contributions from gas cooling and SNIa heating. The simulations show that the values of  $T_{\text{kin}}$  (equation 19) are almost coincident with those of  $T_\sigma$  in the medium- to high- $\sigma_{e8}$  models (i.e. models in a slow inflow where  $\gamma_{\text{th}}$  is very small, see Tables A1 and A2). The low- $\sigma_{e8}$  wind models, instead, have  $T_{\text{kin}} > T_\sigma$ , and the temperature difference is due to thermalization of the strong meridional motions developed in the wind phase ( $T_{\text{kin}} \simeq T_\sigma + T_m$ , while  $T_\varphi$  remains very small). In Fig. 12, it is even more apparent than in Fig. 10 how VD models are in general hotter than their

rotating counterparts, due to the above discussed hydrodynamical effects. In addition, the  $T_X$  difference between VD and IS models increases with galaxy flattening, and it is larger for the more massive and FO-built models, and decreases for smaller and EO-built models. Exceptions are found in the low- $\sigma_{e8}$  EO-built models, as a consequence of the transition to global wind induced by flattening and rotation.

Two interesting considerations can be made by comparing  $T_X$  resulting from the simulations with the temperatures  $T_{\text{kin}}$  and  $T_\sigma$  associated with the thermalization of stellar motions. The first is that  $T_X$  of all models is higher than  $T_{\text{kin}}$  and  $T_\sigma$ , as somewhat

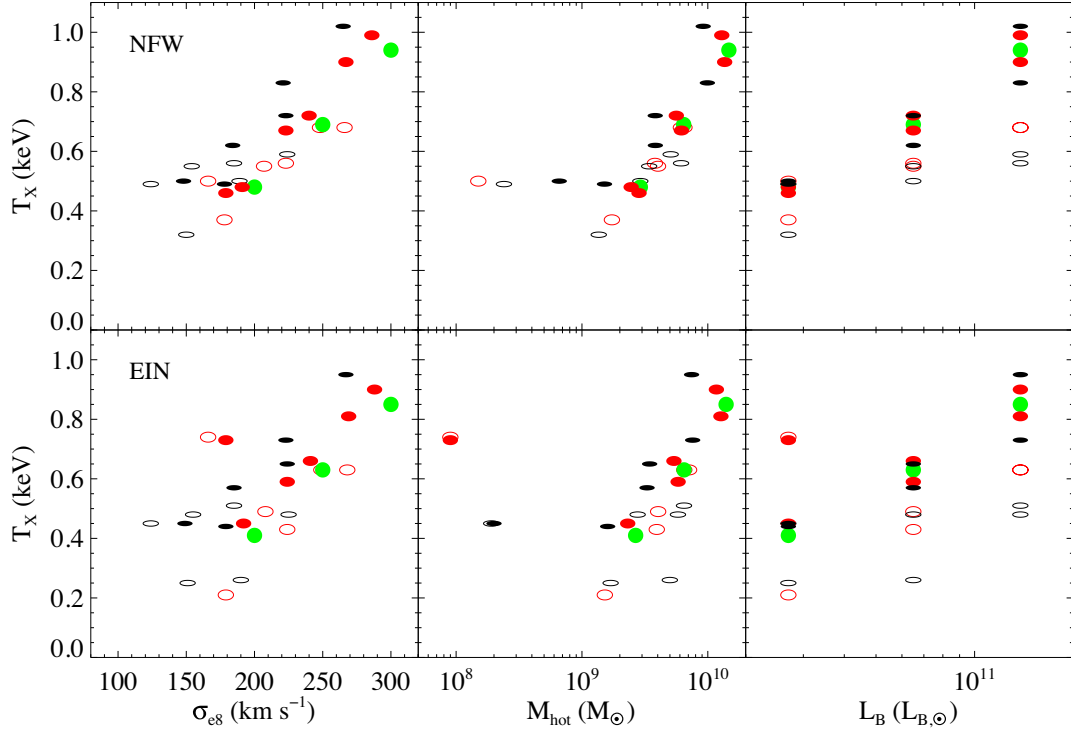


**Figure 10.** Emission-weighted ISM temperature  $T_X$  in the 0.3–8 keV band at 13 Gyr for all the models in the NFW (top panels) and in the Einasto (bottom panels) sets as a function of  $\sigma_{e8}$ , of the hot ( $T > 10^6$  K) ISM mass, and of the galaxy blue optical luminosity. Symbols and colours are as in Fig. 6.

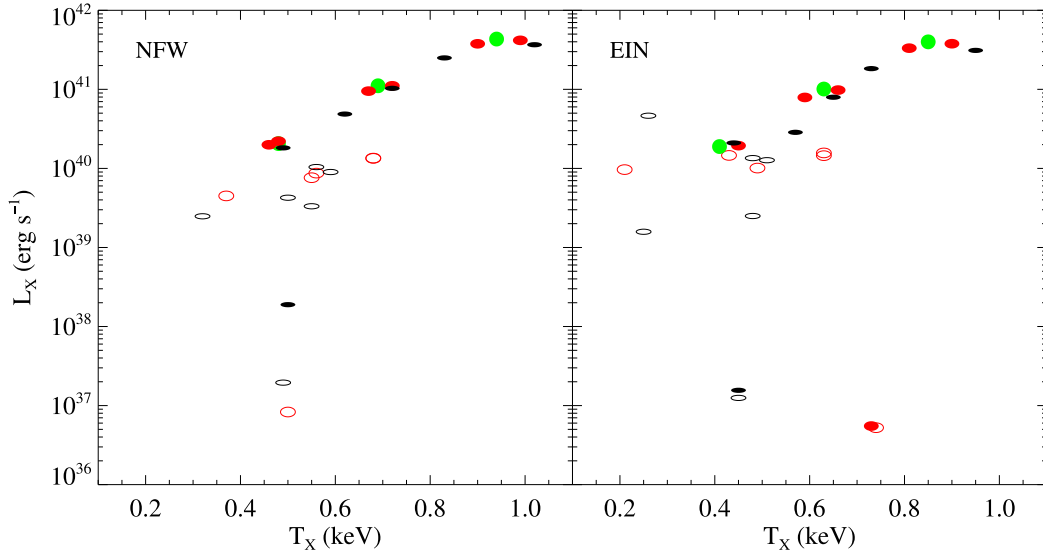


**Figure 11.** X-ray luminosity  $L_X$  with respect to X-ray-luminosity-weighted temperature  $T_X$  at  $t = 13$  Gyr for the whole NFW and Einasto sets. The notation for the symbols is the same as in Fig. 6.

expected due to the additional heating contributions (e.g. from SNIa) to the gas, and to the relatively small radiative losses (we recall that  $T_X$  is computed from the hot, low-density gas only). The second consideration is that, notwithstanding the missing SNIa heating and cooling terms in  $T_\sigma$ , the *trend* of  $T_X$  with galaxy flattening and rotation is the same as that of  $T_\sigma$  for all models, with the exception of the global wind, low- $\sigma_{e8}$  models. Thus,  $T_\sigma$ , except for wind cases, is a good proxy for  $T_{kin}$ , and a robust indicator of the trend of  $T_X$  with galaxy properties (shape and internal kinematics). As a final

comment, we note that, in general, at fixed  $\sigma_{e8}$ , Einasto models tend to be slightly colder than the NFW models, both in  $T_X$  and  $T_\sigma$ , due to the different dark matter profile.

#### 4 DISCUSSION AND CONCLUSIONS

In this paper, in a follow-up of a series of preliminary studies, we performed a large suite of high-resolution 2D hydrodynamical simulations, to study the effects of galaxy shape and stellar kinematics

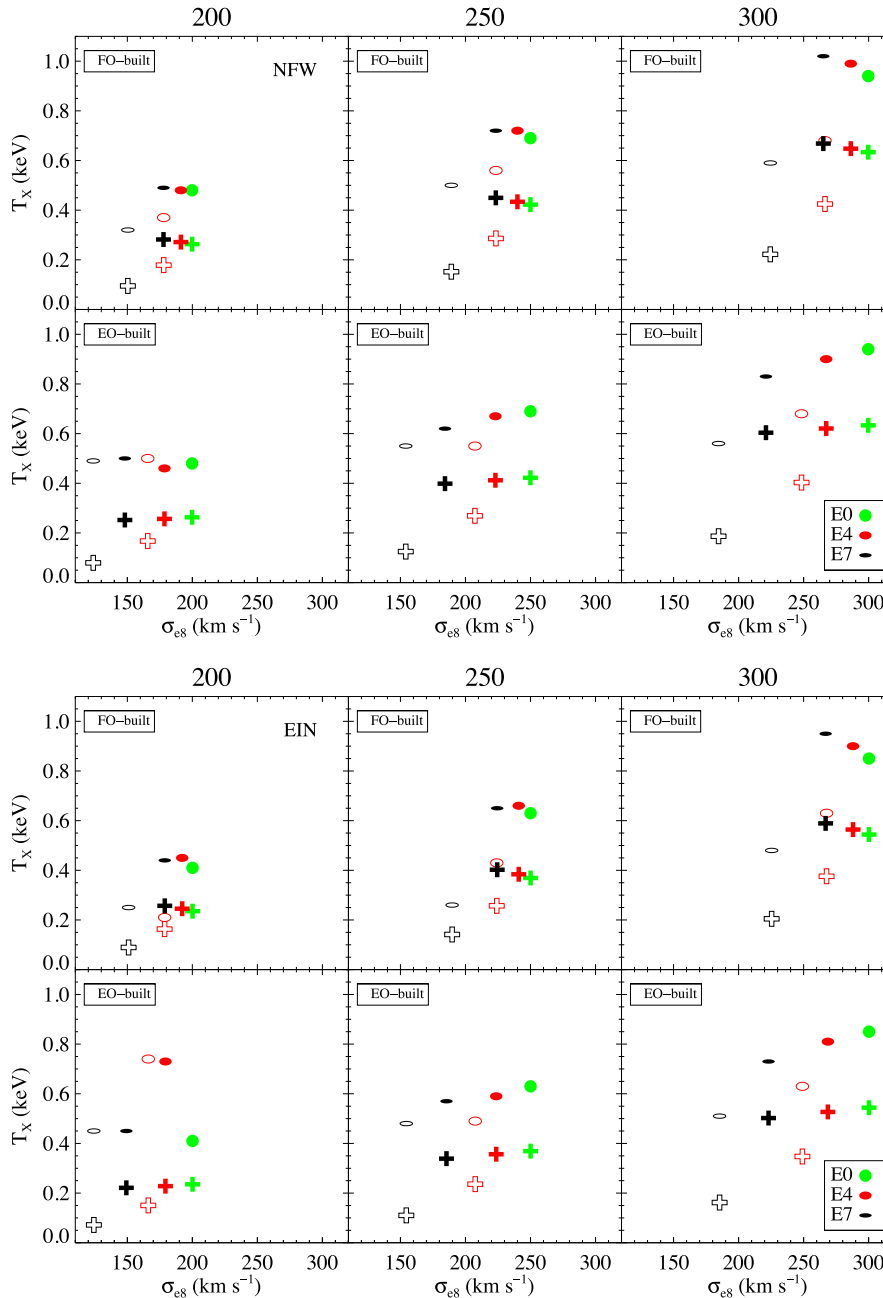


**Figure 12.** The emission-weighted ISM temperature  $T_X$  in the 0.3–8 keV band at 13 Gyr for the models in the NFW (top six panels) and in the Einasto (bottom six panels) sets as a function of  $\sigma_{e8}$ . Different columns show the results for the families obtained from the spherical progenitors with  $\sigma_{e8} = (200, 250, 300)$   $\text{km s}^{-1}$ , and refer to model flattened according to the EO or FO procedure. The green, red and black colours refer to the E0, E4 and E7 models, respectively (progenitors are in green). Filled symbols indicate the fully velocity-dispersion supported VD models, while open symbols indicate the isotropic rotators IS models. Crosses show the values of  $T_\sigma$  calculated according to equation (18). For the relation of  $T_\sigma$  with  $T_{\text{kin}}$  and  $T_X$ , see the Section 2.3.

on the evolution of the X-ray-emitting gaseous haloes of ETGs. Realistic galaxy models are built with a Jeans code, which allows for a full generality in the choice of axisymmetric galaxy shape and of the stellar and dark matter profiles, that can be tailored to reproduce observational constraints. The dynamical structure of the models obeys the implicit assumption of a two-integrals phase-space distribution function. Stellar motions in the azimuthal direction are split among velocity dispersion and ordered rotation by using the Satoh (1980) decomposition. In particular, we explored two extreme kinematical configurations, the fully velocity-

dispersion-supported system (VD) and the isotropic rotator (IS), in order to encompass all the possible behaviours occurring in nature. Of course, the VD configuration applies only to a minor fraction of the flat galaxy population (e.g. Emsellem et al. 2011). Moreover, IS models approximate only to some extent the dynamical structure of flat and fast-rotating galaxies, since the latter are more generally characterized by a varying degree of anisotropy in the meridional plane with intrinsic flattening (Cappellari et al. 2007). The source of gas is provided by secular evolution of the stellar population (stellar winds from ageing stars and SNIa ejecta).

Heating terms account for SNIa events and thermalization of stellar motions.

The main focus of this work is the explanation of long-standing and more recently observed trends of  $L_X$  and  $T_X$  with galaxy shape and rotation (as well as, of course, with fundamental galaxy properties as stellar velocity dispersion and optical luminosity). Pieces of evidence from previous exploratory theoretical (CP96; P13) and numerical works (DC98; N14) seem to point towards a cooperation of flattening and rotation in establishing the final X-ray luminosity and temperature of the ISM. However, which of the two is the driving parameter, and what is the involved physical *mechanism*, had not been clarified yet. From the present investigation, we conclude that more than one physical effect is at play, and that the relative importance of flattening and rotation changes as a function of galaxy mass. We summarize the results discussing first the X-ray luminosity and then the emission-weighted ISM temperature.

(1) In low-mass galaxy models with a progenitor hosting a global wind, the effects of flattening and rotation are just to make the wind stronger, and all systems are found at the lowest values of  $L_X$ .

(2) In the case of galaxies energetically near to the onset of a galactic wind, i.e. for ETGs with  $\sigma_{e8} \approx 200 \text{ km s}^{-1}$ , flattening and rotation contribute significantly to induce a wind, in agreement with the energetic expectations discussed in CP96, with the consequent sharp decrease of  $L_X$ . The transition to a global wind is favoured, respectively, by the facts that flattening can reduce the depth of the potential well, and that in rotating systems the ISM and the stellar component almost corotate; this reduces (in absolute value) the effective potential experienced by the ISM.

(3) In models with  $\sigma_{e8} > 200 \text{ km s}^{-1}$ , galaxy shape variations, in absence of rotation, have only a minor impact on the values of  $L_X$ , in the sense that fully velocity-dispersion-supported flattened models have  $L_X$  similar to or just lower than that of their spherical progenitors.

(4) In flat galaxies with  $\sigma_{e8} > 200 \text{ km s}^{-1}$ , rotation reduces significantly  $L_X$ . Not only the thermalization parameter is low and part of the heating due to stellar motions is missing with respect to the corresponding VD model, but rotation acts also on the hydrodynam-

ics of the gas flow: conservation of angular momentum of the ISM injected at large radii favours gas cooling through the formation of rotating discs of cold gas, reducing the amount of hot gas in the central regions and then  $L_X$ . The effects of angular momentum are clearly visible in Fig. 13, where we show the EO projected X-ray surface brightness maps. In conclusion, galaxy flattening has an important though *indirect* effect for medium- to high-mass galaxies in the sense that only flattened systems can host significant rotation of the stellar component.

(5) The luminosity evolution and the luminosity values at the end of the simulations are similar for the NFW or Einasto dark matter haloes (at fixed stellar structure and similar values of the dark matter halo mass).

The main results concerning the emission-weighted temperature  $T_X$  can be summarized as follows.

(6) As for  $L_X$ , also for  $T_X$  the response to a variation of shape and internal kinematics is different for low- and high-mass galaxies.  $T_X$  does not change appreciably adding flattening and rotation to low-mass progenitors that are in the global wind phase. Due to their low density and high meridional velocities, global winds are generally hotter than that expected by extrapolation of the  $T_X$  of more massive systems. As described at point (2) above, adding flattening and rotation to ETGs energetically near to host a global wind leads to a transition to a wind phase, with the consequent increase of  $T_X$ .

(7) In the medium- to high-mass galaxies, a change of shape produces small changes in  $T_X$ . Adding rotation, instead, results in a much lower  $T_X$ . This is because angular momentum conservation leads to the formation of a massive centrifugally supported cold disc and to a lower density of the hot ISM in the central regions above and below the equatorial plane, with respect to VD models. Then, the external, and colder, regions weight more in the computation of  $T_X$ .

(8) Overall, for medium- to high-mass galaxies,  $T_X$  increases with galaxy mass, independently of the specific dark matter halo profile. In general, in the Einasto haloes, the hot gas is systematically cooler and with a larger scatter in  $T_X$  than in the NFW dark matter haloes of comparable mass.

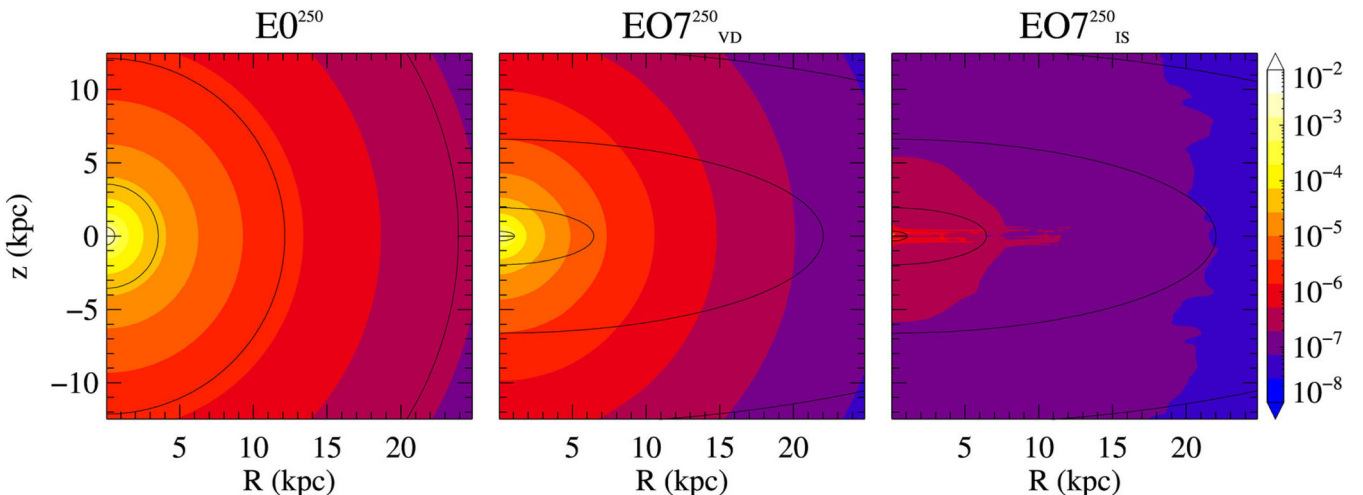


**Figure 13.** EO 0.3–8 keV surface brightness of the ISM ( $\Sigma_X$ ) at 13 Gyr, for  $\text{EO}^{250}$ ,  $\text{EO7}_{\text{VD}}^{250}$  and  $\text{EO7}_{\text{IS}}^{250}$  models, respectively; the brightness values on the colour bar are given in  $\text{erg s}^{-1} \text{cm}^{-2}$ . Superimposed are the isophotes ( $\Sigma_*$ ) obtained by projecting the galaxy stellar density distribution, with the innermost contour corresponding to  $10^4 M_{\odot} \text{pc}^{-2}$ , and decreasing by a factor of 10 on each subsequent contour going outwards. Note that the  $\Sigma_X$  map of the  $\text{EO7}_{\text{VD}}^{250}$  model shows a round shape and a luminous core very similar to the  $\text{EO}^{250}$  map, whereas  $\text{EO7}_{\text{IS}}^{250}$  map presents a boxy shape and a low-luminosity core.

(9) In rotating models, the ISM almost corotates with the stars, and so there is a corresponding reduction of the thermalization of the galaxy streaming velocity. At the same time, the rotating ISM is less bound, due to the centrifugal support. With the exception of low-mass galaxies in the wind phase,  $T_\sigma$  (the temperature associated with the thermalization of the stellar velocity dispersion) is a good proxy for  $T_{\text{kin}}$ , the true thermalization temperature of stellar motions, as computed from the simulations; for wind models, instead,  $T_{\text{kin}} > T_\sigma$ . In general,  $T_X > T_{\text{kin}}$ , but the qualitative dependence of  $T_X$  on galaxy mass and shape in no-wind galaxies is very well reproduced by that of  $T_\sigma$ , a quantity that can be computed without resorting to numerical simulations.

A few important physical phenomena are still missing from the simulations. First, it is obvious that in rotationally supported models the massive and rotating cold discs are natural places for star formation. For observational studies, it would be interesting to estimate age and mass of the new stars. From the point of view of the present investigation, the formation of stars, by reducing the amount of cold gas in the equatorial plane, could in principle also modify the evolution of the ISM. We performed a few tests where we activated star formation at a rate  $\dot{\rho}_*$ , following Ciotti & Ostriker (2012) and references therein:

$$\dot{\rho}_* = \eta \frac{\rho}{t_{\text{form}}}, \quad t_{\text{form}} = \max(t_{\text{cool}}, t_{\text{dyn}}), \quad (20)$$

where  $0.01 \leq \eta \leq 0.1$ ,  $t_{\text{cool}} = E/\mathcal{L}$  (equation 9) and  $t_{\text{dyn}} \propto 1/\sqrt{G\rho}$ . In the test simulations for the model FO7<sub>IS</sub><sup>300</sup> of the NFW set, star formation peaks at the first 3–4 Gyr with a rate of  $\approx 10 M_\odot \text{ yr}^{-1}$ , and the final mass in the new stellar disc is of the order of  $\text{few} \times 10^{10} M_\odot$ ; most of the gas disc is consumed by star formation. No significant effects are produced on the ISM luminosity and temperature, so that from this point of view the present results can be considered robust. However, in the test simulations, star formation was activated in a ‘passive’ fashion, i.e. only gas subtraction from the computational domain was considered, so that the injection of mass, momentum and energy due to the evolution of the new stars was not included; these effects will be considered in a future work. An interesting link between our finding of an ubiquitous formation of a cold disc in rotating systems and observed galaxy properties is given by the fact that, among ETGs, it is only in fast rotators that some degree of star formation is observed (Davis et al. 2011; Young et al. 2011; Sarzi et al. 2013).

A second aspect missing here is the self-gravity of the gaseous cold disc. It is expected that self-gravity acts not only to promote star formation, but also to develop non-axisymmetric instabilities, which lead to non-conservation of angular momentum of the gas. Phenomenologically, the effects of self-gravity can be viewed as a ‘gravitational viscosity’ (e.g. Bertin & Lodato 2001), which favours accretion of cold gas towards the centre. Such a gas flow towards the centre is of great importance for feedback effects from a central massive black hole in rotating galaxies (Novak, Ostriker & Ciotti 2011; Gan et al. 2014). In a complementary exploration, we are currently studying the interplay between the ISM of a rotating galaxy on large scale and the feedback effects from the central black hole.

## ACKNOWLEDGEMENTS

We thank the anonymous referee for constructive comments. LC acknowledges Giuseppe Bertin, Jerry and Eve Ostriker, and James Stone for useful discussions. LC and SP were supported by the MIUR grant PRIN 2010-2011, project ‘The Chemical and Dynamical Evolution of the Milky Way and Local Group Galaxies’, prot. 2010LY5N2T.

## REFERENCES

- Behroozi P. S., Wechsler R. H., Conroy C., 2013, *ApJ*, 770, 57  
 Bertin G., Lodato G., 2001, *A&A*, 370, 342  
 Boroson B., Kim D.-W., Fabbiano G., 2011, *ApJ*, 729, 12  
 Brighenti F., Mathews W. G., 1996, *ApJ*, 470, 747  
 Cappellari M. et al., 2007, *MNRAS*, 379, 418  
 Ciotti L., Ostriker J. P., 2012, in Kim D.-W., Pellegrini S., eds, *Astrophysics and Space Science Library*, Vol. 378, *Hot Interstellar Matter in Elliptical Galaxies*. Springer-Verlag, Berlin, p. 83  
 Ciotti L., Pellegrini S., 1996, *MNRAS*, 279, 240 (CP96)  
 Davis T. A. et al., 2011, *MNRAS*, 417, 882  
 de Vaucouleurs G., 1948, *Ann. Astrophys.*, 11, 247  
 D’Ercole A., Ciotti L., 1998, *ApJ*, 494, 535 (DC98)  
 Desroches L.-B., Quataert E., Ma C.-P., West A. A., 2007, *MNRAS*, 377, 402  
 Einasto J., 1965, *Tr. Astrofiz. Inst. Alma-Ata*, 5, 87  
 Emsellem E. et al., 2011, *MNRAS*, 414, 888  
 Eskridge P. B., Fabbiano G., Kim D.-W., 1995, *ApJS*, 97, 141  
 Fabbiano G., 1989, *ARA&A*, 27, 87  
 Gan Z., Yuan F., Ostriker J. P., Ciotti L., Novak G. S., 2014, *ApJ*, 789, 150  
 Kim D.-W., Pellegrini S. eds, 2012, *Astrophysics and Space Science Library*, Vol. 378, *Hot Interstellar Matter in Elliptical Galaxies*. Springer-Verlag, Berlin  
 Li J.-T., Wang Q. D., Li Z., Chen Y., 2011, *ApJ*, 737, 41  
 Maraston C., 2005, *MNRAS*, 362, 799  
 Mathews W. G., Brighenti F., 2003, *ARA&A*, 41, 191  
 Mellier Y., Mathez G., 1987, *A&A*, 175, 1  
 Navarro J. F., Frenk C. S., White S. D. M., 1997, *ApJ*, 490, 493  
 Negri A., Ciotti L., Pellegrini S., 2014, *MNRAS*, 439, 823 (N14)  
 Novak G. S., Ostriker J. P., Ciotti L., 2011, *ApJ*, 737, 26  
 O’Sullivan E., Forbes D. A., Ponman T. J., 2001, *MNRAS*, 324, 420  
 Parriott J. R., Bregman J. N., 2008, *ApJ*, 681, 1215  
 Pellegrini S., 1999, *A&A*, 351, 487  
 Pellegrini S., 2011, *ApJ*, 738, 57  
 Pellegrini S., 2012, in Kim D.-W., Pellegrini S., eds, *Astrophysics and Space Science Library*, Vol. 378, *Hot Interstellar Matter in Elliptical Galaxies*. Springer-Verlag, Berlin, p. 21  
 Pellegrini S., Held E. V., Ciotti L., 1997, *MNRAS*, 288, 1  
 Posacki S., Pellegrini S., Ciotti L., 2013, *MNRAS*, 433, 2259 (P13)  
 Retana-Montenegro E., van Hese E., Gentile G., Baes M., Frutos-Alfaro F., 2012, *A&A*, 540, A70  
 Sarzi M. et al., 2010, *MNRAS*, 402, 2187  
 Sarzi M. et al., 2013, *MNRAS*, 432, 1845  
 Satoh C., 1980, *PASJ*, 32, 41  
 Sazonov S. Y., Ostriker J. P., Ciotti L., Sunyaev R. A., 2005, *MNRAS*, 358, 168  
 Smith R. K., Brickhouse N. S., Liedahl D. A., Raymond J. C., 2001, *ApJ*, 556, L91  
 Young L. M. et al., 2011, *MNRAS*, 414, 940

## APPENDIX A: TABLES

**Table A1.** Simulation results for the NFW set at  $t = 13$  Gyr.

Name	$M_{\text{inj}}$ ( $10^9 M_{\odot}$ )	$M_{\text{esc}}$ ( $10^9 M_{\odot}$ )	$M_{\text{gas}}$ ( $10^9 M_{\odot}$ )	$M_{\text{hot}}$ ( $10^9 M_{\odot}$ )	$L_X$ ( $10^{40} \text{ erg s}^{-1}$ )	$T_X$ (keV)	$L_{\text{SN}}$ ( $10^{40} \text{ erg s}^{-1}$ )	$T_{\text{kin}}$ (keV)	$T_{\sigma}$ (keV)	$T_v$ (keV)	$T_m$ (keV)	$\gamma_{\text{th}}$	$\gamma_{\text{th}}^{\phi}$
(1)	(2)	(3)	(4)	(5)	(6)	(7)	(8)	(9)	(10)	(11)	(12)	(13)	(14)
E0 <sup>200</sup>	12.0	3.2	8.9	2.91	2.06	0.48	10.2	0.26	0.26	1.7E−3	1.7E−3	–	–
EO4 <sup>200</sup> <sub>IS</sub>	11.9	9.8	2.4	0.15	8.29E−4	0.50	10.2	0.40	0.17	0.24	0.21	2.62	0.25
EO4 <sup>200</sup> <sub>VD</sub>	11.9	4.5	7.5	2.84	1.99	0.46	10.2	0.26	0.26	1.5E−3	1.5E−3	–	–
EO7 <sup>200</sup> <sub>IS</sub>	11.9	10.3	1.8	0.24	1.95E−3	0.49	10.2	0.29	0.08	0.22	0.18	1.24	0.22
EO7 <sup>200</sup> <sub>VD</sub>	11.9	9.4	2.8	0.66	1.89E−2	0.50	10.2	0.33	0.25	7.8E−2	7.8E−2	–	–
FO4 <sup>200</sup> <sub>IS</sub>	12.0	3.3	8.8	1.73	0.45	0.37	10.3	0.21	0.18	2.9E−2	9.0E−3	0.31	0.21
FO4 <sup>200</sup> <sub>VD</sub>	12.0	2.9	9.2	2.46	2.21	0.48	10.3	0.27	0.27	3.7E−3	3.7E−3	–	–
FO7 <sup>200</sup> <sub>IS</sub>	12.0	3.4	8.7	1.36	0.25	0.32	10.2	0.12	0.09	2.9E−2	1.1E−2	0.15	0.10
FO7 <sup>200</sup> <sub>VD</sub>	12.0	4.0	8.1	1.51	1.82	0.49	10.2	0.28	0.28	2.0E−3	2.0E−3	–	–
E0 <sup>250</sup>	32.2	5.1	27.5	6.43	11.1	0.69	24.3	0.42	0.42	1.2E−3	1.2E−3	–	–
EO4 <sup>250</sup> <sub>IS</sub>	31.7	8.3	23.8	4.02	0.76	0.55	23.9	0.29	0.27	1.8E−2	3.1E−3	0.13	0.10
EO4 <sup>250</sup> <sub>VD</sub>	31.7	6.9	25.2	6.17	9.50	0.67	23.9	0.42	0.41	1.5E−3	1.5E−3	–	–
EO7 <sup>250</sup> <sub>IS</sub>	30.6	11.4	19.7	3.42	0.33	0.55	23.1	0.18	0.13	5.5E−2	4.9E−3	0.20	0.18
EO7 <sup>250</sup> <sub>VD</sub>	30.6	12.5	18.7	3.83	4.87	0.62	23.1	0.41	0.40	1.8E−3	1.8E−3	–	–
FO4 <sup>250</sup> <sub>IS</sub>	32.2	6.5	26.2	3.80	0.87	0.56	24.3	0.30	0.29	1.9E−2	3.9E−3	0.13	0.10
FO4 <sup>250</sup> <sub>VD</sub>	32.2	5.2	27.4	5.62	11.1	0.72	24.3	0.43	0.43	1.6E−3	1.6E−3	–	–
FO7 <sup>250</sup> <sub>IS</sub>	32.2	6.4	26.0	2.91	0.43	0.50	24.2	0.19	0.15	3.7E−2	7.9E−3	0.13	0.10
FO7 <sup>250</sup> <sub>VD</sub>	32.2	7.4	25.3	3.82	10.3	0.72	24.2	0.45	0.45	1.7E−3	1.7E−3	–	–
E0 <sup>300</sup>	71.3	7.6	64.7	14.70	43.3	0.94	49.1	0.65	0.65	1.0E−3	1.0E−3	–	–
EO4 <sup>300</sup> <sub>IS</sub>	69.4	14.1	56.0	6.52	1.34	0.68	47.7	0.43	0.42	1.5E−2	1.9E−3	0.07	0.06
EO4 <sup>300</sup> <sub>VD</sub>	69.4	10.5	59.9	13.61	37.7	0.90	47.7	0.63	0.63	1.2E−3	1.2E−3	–	–
EO7 <sup>300</sup> <sub>IS</sub>	65.5	15.9	50.2	6.13	1.04	0.56	45.0	0.23	0.20	2.3E−2	1.5E−3	0.06	0.05
EO7 <sup>300</sup> <sub>VD</sub>	65.5	17.8	48.8	9.92	25.0	0.83	45.0	0.62	0.62	1.2E−3	1.2E−3	–	–
FO4 <sup>300</sup> <sub>IS</sub>	71.8	11.9	60.9	6.11	1.35	0.68	49.4	0.45	0.43	1.7E−2	4.0E−3	0.08	0.06
FO4 <sup>300</sup> <sub>VD</sub>	71.8	8.5	64.3	12.91	41.7	0.99	49.4	0.65	0.65	1.5E−3	1.5E−3	–	–
FO7 <sup>300</sup> <sub>IS</sub>	71.9	11.1	61.8	5.07	0.90	0.59	49.5	0.25	0.23	2.7E−2	4.0E−3	0.06	0.05
FO7 <sup>300</sup> <sub>VD</sub>	71.9	12.7	60.4	9.19	36.7	1.02	49.5	0.67	0.67	1.6E−3	1.6E−3	–	–

*Notes:* (1) Name of the model. (2)–(3) Total ISM mass injected into and escaped from the numerical grid, respectively. Differences in  $M_{\text{inj}}$  for models of same  $L_B$  are accounted for different sampling of  $\rho_*$  over the numerical grid. (4) Total ISM mass retained within the galaxy at the end of the simulation. (5)–(7) ISM mass with  $T > 10^6$  K, ISM X-ray luminosity in the 0.3–8 keV band and ISM X-ray-emission-weighted temperature in the same band, at the end of the simulation. (8) SNIa heating rate at the end of the simulation. (9)–(12) Thermalization temperatures of stellar motions at the end of the simulation, defined accordingly to equations (19) and (18). By construction,  $T_{\text{kin}} = T_{\sigma} + T_v$ ; for rotating models  $T_v = \gamma_{\text{th}} T_{\text{rot}}$  and  $T_{\phi} = T_v - T_m = \gamma_{\text{th}}^{\phi} T_{\text{rot}}$ , while for velocity-dispersion-supported models,  $T_v = T_m$  (see Section 2.3). (13)–(14) Thermalization parameter as defined in equation (15), and its azimuthal component  $\gamma_{\text{th}}^{\phi} = L_{\phi}/L_{\text{rot}}$  (see equation 14), at the end of the simulation.

**Table A2.** Simulation results for the Einasto set at  $t = 13$  Gyr.

Name	$M_{\text{inj}}$ ( $10^9 M_{\odot}$ )	$M_{\text{esc}}$ ( $10^9 M_{\odot}$ )	$M_{\text{gas}}$ ( $10^9 M_{\odot}$ )	$M_{\text{hot}}$ ( $10^9 M_{\odot}$ )	$L_X$ ( $10^{40} \text{ erg s}^{-1}$ )	$T_X$ (keV)	$L_{\text{SN}}$ ( $10^{40} \text{ erg s}^{-1}$ )	$T_{\text{kin}}$ (keV)	$T_{\sigma}$ (keV)	$T_v$ (keV)	$T_m$ (keV)	$\gamma_{\text{th}}$	$\gamma_{\text{th}}^{\phi}$
(1)	(2)	(3)	(4)	(5)	(6)	(7)	(8)	(9)	(10)	(11)	(12)	(13)	(14)
EO <sup>200</sup>	12.0	3.9	8.2	2.67	1.89	0.41	10.2	0.24	0.24	3.7E−3	3.7E−3	−	−
EO4 <sup>200</sup> <sub>IS</sub>	11.9	12.1	0.1	0.09	5.25E−4	0.74	10.2	0.49	0.15	0.34	0.31	4.34	0.28
EO4 <sup>200</sup> <sub>VD</sub>	11.9	12.1	0.1	0.09	5.51E−4	0.73	10.2	0.54	0.23	0.31	0.31	−	−
EO7 <sup>200</sup> <sub>IS</sub>	11.9	12.0	0.2	0.19	1.25E−3	0.45	10.2	0.34	0.07	0.27	0.24	1.79	0.14
EO7 <sup>200</sup> <sub>VD</sub>	11.9	11.3	0.9	0.20	1.56E−3	0.45	10.2	0.42	0.22	0.20	0.20	−	−
FO4 <sup>200</sup> <sub>IS</sub>	12.0	6.0	5.7	1.52	0.97	0.21	10.3	0.21	0.16	5.2E−2	2.1E−2	0.63	0.37
FO4 <sup>200</sup> <sub>VD</sub>	12.0	3.6	8.5	2.31	1.94	0.45	10.3	0.25	0.25	2.1E−3	2.1E−3	−	−
FO7 <sup>200</sup> <sub>IS</sub>	12.0	3.9	8.2	1.69	0.16	0.25	10.2	0.14	0.09	4.8E−2	3.0E−2	0.28	0.11
FO7 <sup>200</sup> <sub>VD</sub>	12.0	4.9	7.3	1.60	2.10	0.44	10.2	0.26	0.26	2.8E−3	2.8E−3	−	−
EO <sup>250</sup>	32.2	6.6	26.0	6.47	10.1	0.63	24.3	0.37	0.37	1.4E−3	1.4E−3	−	−
EO4 <sup>250</sup> <sub>IS</sub>	31.7	10.3	21.8	4.03	1.01	0.49	23.9	0.26	0.24	1.8E−2	3.4E−3	0.15	0.12
EO4 <sup>250</sup> <sub>VD</sub>	31.7	9.2	22.9	5.81	7.90	0.59	23.9	0.36	0.36	1.9E−3	1.9E−3	−	−
EO7 <sup>250</sup> <sub>IS</sub>	30.6	14.2	16.9	2.77	0.25	0.48	23.1	0.18	0.11	6.2E−2	9.4E−3	0.27	0.26
EO7 <sup>250</sup> <sub>VD</sub>	30.6	16.0	15.2	3.29	2.86	0.57	23.1	0.35	0.34	3.2E−3	3.2E−3	−	−
FO4 <sup>250</sup> <sub>IS</sub>	32.2	8.1	24.5	3.93	1.46	0.43	24.3	0.27	0.26	1.7E−2	3.8E−3	0.13	0.10
FO4 <sup>250</sup> <sub>VD</sub>	32.2	6.9	25.8	5.38	9.79	0.66	24.3	0.38	0.38	2.0E−3	2.0E−3	−	−
FO7 <sup>250</sup> <sub>IS</sub>	32.2	8.0	24.4	4.99	4.64	0.26	24.2	0.17	0.14	2.9E−2	1.1E−2	0.11	0.07
FO7 <sup>250</sup> <sub>VD</sub>	32.2	9.5	23.3	3.45	7.95	0.65	24.2	0.40	0.40	2.0E−3	2.0E−3	−	−
EO <sup>300</sup>	71.3	9.6	62.7	13.97	39.9	0.85	49.1	0.56	0.56	1.0E−3	1.0E−3	−	−
EO4 <sup>300</sup> <sub>IS</sub>	69.4	17.2	53.2	7.10	1.57	0.63	47.7	0.38	0.36	1.5E−2	1.6E−3	0.09	0.08
EO4 <sup>300</sup> <sub>VD</sub>	69.4	13.0	57.5	12.71	33.2	0.81	47.7	0.54	0.54	1.4E−3	1.4E−3	−	−
EO7 <sup>300</sup> <sub>IS</sub>	65.5	20.3	45.6	6.47	1.27	0.51	45.0	0.20	0.18	2.6E−2	2.2E−3	0.08	0.07
EO7 <sup>300</sup> <sub>VD</sub>	65.5	23.5	43.2	7.58	18.3	0.73	45.0	0.52	0.52	1.8E−3	1.8E−3	−	−
FO4 <sup>300</sup> <sub>IS</sub>	71.8	14.5	58.0	6.50	1.45	0.63	49.4	0.40	0.38	1.8E−2	3.6E−3	0.10	0.08
FO4 <sup>300</sup> <sub>VD</sub>	71.8	11.1	61.8	11.70	37.8	0.90	49.4	0.57	0.57	1.7E−3	1.7E−3	−	−
FO7 <sup>300</sup> <sub>IS</sub>	71.9	14.1	56.6	5.79	1.35	0.48	49.5	0.23	0.21	2.5E−2	3.5E−3	0.07	0.06
FO7 <sup>300</sup> <sub>VD</sub>	71.9	16.9	56.3	7.43	31.1	0.95	49.5	0.60	0.59	1.8E−3	1.8E−3	−	−

Notes: All quantities are as in Table A1.

This paper has been typeset from a  $\text{\LaTeX}$  file prepared by the author.